ApoE isoforms differentially regulate neuronal membrane proteasomes to shift the threshold for pathological aggregation of endogenous Tau

Paradise V[1,2], Sabu M[1,2], Bafia J[3], Sharif NA[1,2], Nguyen C[1,2], Dhanraj Mukim R[1,2], Wang X[1,2], Fu J[4], Ndubisi J[1,2], Maldonado G[1,2], Strickland M[5], Figueroa H[1], Almeida D[1,2], Hyman B[6], Holtzman DM[5], Nuriel T[1], Ramachandran KV[1,2,7]*

1 Taub Institute for Research on Alzheimer's Disease and the Aging Brain, Columbia University Vagelos College of Physicians and Surgeons, New York, NY 10032
Taub Institute for Research on Alzheimers Disease and the Aging Brain, Columbia University Vagelos College of Physicians and Surgeons, New York, NY 10032
2 Department of Neurology, Columbia University Irving Medical Center. New York, NY 10032
3 Department of Molecular and Cellular Biology, Harvard University, Cambridge, MA 02139
4 Program in Medical and Population Genetics, Broad Institute of MIT and Harvard, Cambridge, MA
5 Department of Neurology, Developmental Biology, Hope Center for Neurological Disorders, Alzheimers Disease Research Center, Washington University School of Medicine, St. Louis, MO 63110
6 Alzheimer Research Unit of the MassGeneral Institute for Neurodegenerative Disease, Department of Neurology of the Massachusetts General Hospital, and Harvard Medical School, Charlestown, Massachusetts 02129-4404
7 Department of Neuroscience, Columbia University Vagelos College of Physicians and Surgeons, New York, NY 10032

*To whom correspondence should be addressed: kvr2113@cumc.columbia.edu

Neuronal membrane proteasomes (NMPs) are a functionally transmembrane subset of 20S proteasomes that degrade newly synthesized proteins. To date, the molecular composition of NMPs is undefined, and moreover, whether NMPs can influence any aspect of protein aggregation with relevance to neurodegenerative disorders remains unexplored. Using a Cre-dependent conditional knock-in mouse line to endogenously tag the proteasome, we find that NMPs co-purify with ApoE. We discover that NMP membrane localization is differentially modulated by ApoE isoforms (E4<E3<E2) *in vitro*, *in vivo*, and in human postmortem samples. This isoform-dependent change in NMP localization inversely correlates with the risk that ApoE isoforms pose for Alzheimer's Disease. ApoE4-dependent reduction of NMP localization is strongest in brain regions selectively vulnerable to neurodegeneration. We synthesized selective NMP-specific inhibitors and discovered that NMP inhibition induces aggregation of endogenous and newly synthesized mouse and human Tau isoforms, without the need for seeding or pathogenic mutations. We posit that newly synthesized Tau is exceptionally susceptible to aggregation due to NMP dysfunction. Stereotactic injection of NMP inhibitors *in vivo* induces aggregation, phosphorylation, somatodendritic mislocalization and pathology of endogenous newly synthesized Tau. Finally, using ApoE-KI/hTau-KI crosses, we find that ApoE isoforms differentially shift the aggregation threshold for Tau. Overall, our data define NMPs as a pivotal

proteostasis mechanism underlying the formation of endogenous Tau aggregates, which is directly regulated by the largest genetic risk factor for late-onset Alzheimer's Disease.

Introduction

All cells require the faithful spatiotemporal control of protein degradation. In the canonical models of protein degradation, proteins are either degraded by the ubiquitin-proteasome system or the endo-lysosomal and autophagic systems[1,2]. We recently described a neuronal-specific system for protein degradation: a proteasome which is functionally transmembrane[3]. Neuronal membrane proteasomes, or NMPs, are localized to the neuronal plasma membrane, degrade intracellular substrates across the membrane, and are exposed to the extracellular space[3]. The NMP does not contain the 19S cap, and instead has been demonstrated to co- or peri-translationally degrade proteins across the membrane without the need for ubiquitylation[4]. As these are relatively newly described complexes, very little is understood about their composition or function.

Alzheimer's Disease (AD) and many other neurodegenerative diseases are linked by the accumulation of protein aggregates[5,6]. Tau aggregates are among the most common intracellular aggregates in AD and are characteristic of more than 20 neurodegenerative diseases, termed Tauopathies[7]. The molecular triggers for aggregate formation remain elusive. Multiple mutations that render Tau more prone to aggregation have been identified in patients[8]. Aggregated Tau can induce the further aggregation of otherwise normal Tau, creating a feed-forward prion-like propagation[9-11]. However, much less is known about the protein quality control mechanisms in neurons that prevent endogenous Tau from aggregating in the absence of pathogenic mutations or Tau seeds[12,13]. Tau overexpression is not a cause of AD or other tauopathies, and Tau mutations are only found in rare cases of frontotemporal dementia[14]. The vast majority of Tau aggregates in AD form sporadically[15,16], therefore identifying mechanisms by which Tau aggregates form could provide a unique therapeutic opportunity for intervention before Tau seeds can promote further templating and propagation.

While studies have clearly demonstrated how aggregated Tau affects proteasomal function[17,18], the data for how the proteasome affects Tau aggregates are much more obscure. Proteasomal inhibition in neurons or in the brain does not induce de novo Tau aggregation, confounded by the fact that proteasomal inhibition induces autophagy [19-22]. In fact, generally proteasomal inhibition induces the reduction of soluble Tau through this mechanism [19-22]. However, proteasomes can be involved in clearing already aggregated Tau with the help of ATPases such as VCP or those in the 19S cap[23]. The role for NMPs in Tau turnover remains unexplored. Moreover, the interaction and balance between degradation mechanisms in determining both the formation and clearance of Tau are still debated. Understanding these mechanisms will provide invaluable insights into how and when Tau should be targeted by therapies.

While the precise mechanisms underlying Tau aggregation are still debated, one major genetic factor that influences Tau aggregation and deposition is ApoE[24-26]. The most significant risk factor for late-onset Alzheimer's Disease is the ApoE4 isoform of the ApoE gene, while the ApoE3 isoform is neutral and the ApoE2 isoform is protective[27,28]. The mechanisms by which ApoE isoforms confer these dramatic differences in the risk for AD remains unclear. Even more specifically, it remains mechanistically vague how ApoE isoform influence Tau aggregation. Gaining the biochemical and cell biological insights connecting ApoE isoforms and Tau turnover could be invaluable to revealing the mechanisms underlying neurodegeneration.

Here, we discover an unexpected link between ApoE and Tau catabolism through the newly discovered NMP. Using a transgenic mouse line to endogenously and conditionally tag the 20S proteasome, we found that NMPs co-purify with ApoE. NMP localization at the plasma membrane is differentially regulated by ApoE isoforms, with ApoE4 reducing localization and ApoE2 increasing localization relative to ApoE3, *in vivo*, *in vitro*, and in humans. Using an unbiased quantitative proteomic screen, we identify neuronal responses to NMP inhibition in the soluble and insoluble proteome. The profile of NMP-induced deficits in proteostasis closely mirror proteomic signatures observed in the human AD brain. We find that NMP inhibition induces aggregation of endogenous and newly synthesized Tau, suggesting a new species of Tau that is specifically susceptible to aggregation. NMP-inhibition induced effects on newly synthesized endogenous Tau are observed in WT neurons as well as hTau-KI neurons and *in vivo*, indicative of a broad underlying mechanism. NMP-inhibition-induced Tau aggregates migrate as a high molecular weight species, which is typically reported in the AD brain or with seeding-competent Tau, but more rarely with endogenous Tau. Using quantitative phosphoproteomic analysis supported by imaging *in vitro* in primary neurons and *in vivo* following stereotactic delivery, we find that NMP inhibition induces that phosphorylation of Tau at sites consistent with pathological aggregated Tau in the AD brain. Finally, we find that ApoE4 reduces the threshold at which Tau aggregates by ~ 50-fold compared to ApoE3 and ~200-fold compared to ApoE2, thereby dramatically elevating risk for Tau aggregation. We suggest that NMPs serve as a pivotal proteostasis factor, mechanistically distinct from known degradation systems, directly linking ApoE isoform-dependent risk for AD with Tau aggregation.

Results

Endogenous affinity tags on the 20S proteasome reveal that NMPs co-purify with ApoE and LRP1

We sought to purify the plasma-membrane-bound NMP directly out of the mouse brain. Our attempts to do this out of native tissue proved challenging due to the length of the preparations which caused low yields. To circumvent this, we built a transgenic mouse line to tag the endogenous 20S proteasome for affinity purification. Modifying the 20S allows us to isolate any complex containing the core proteasome, such as free 20S, singly-capped 26S, or doubly-capped

30S proteasomes. We conducted extensive optimization in HEK293T cells and primary neurons by modifying the C-termini of nearly every core proteasome subunit with either 6X-His or Strep-II tags (**Fig S1A**). After screening out constructs based on low expression and removing any that interfered with proteasome function **(Fig S1A)**, we selected subjected remaining constructs to ATPase assays to measure the assembled state of the proteasome (**Fig S1B**). Of the remaining two constructs, we found that only the C-terminal modification of PSMA3 was compatible with proper proteasome assembly, function, and did not adversely affect cell health. Based on these data, we generated a 20S-FLAG transgenic line by adding flanking loxP sites surrounding the final exon (Exon 11) of the PSMA3 gene and then the same sequence with a linker containing a 3X-FLAG tag (**Fig 1A**). By crossing these mice with those expressing Cre recombinase driven by the Baf53b promoter[29], we generated mice that expressed 3XFLAG-tagged proteasomes selectively in the brain (**Fig 1B**). Brains from Baf53b-Cre mice (WT) and Baf53b-Cre/20S-FLAG transgene (Tg) littermate controls were processed to obtain the cytosolic fraction and FLAG-tagged proteasomes were isolated on beads with a nanobody against the FLAG epitope. Simultaneously, 26S proteasomes were isolated using the GST-UBL affinity isolation method and all samples were immunoblotted using antibodies raised against multiple 19S and 20S subunits. We find efficient FLAG affinity isolation of the entire proteasome complex (20S and 26S) and also find that the FLAG tag is incorporated into the 26S proteasome (**Fig 1B**). We fail to detect any FLAG in the littermate controls without Cre (**Fig 1B**). We also measured the catalytic activity of the FLAG epitope-tagged proteasome compared to wild-type proteasomes from the brain by monitoring the cleavage of a model substrate, Suc-LLVY-AMC. An increase in fluorescence reflects the proteasome-dependent cleavage of this LLVY substrate which mobilizes the free fluorescence of AMC. Using LLVY-based proteasome activity assays, we find that the catalytic activity of isolated 26S proteasomes from 20S-FLAG mice are indistinguishable from the proteasomes isolated from WT controls (**Fig 1C**). Next, we find that affinity isolation against the FLAG tag only yields proteasomes from the transgenic animals, and not WT control animals. We find that FLAG affinity purified proteasomes are catalytically identical to 26S affinity isolated proteasomes. These extensive characterizations confirm that epitope tagging of the 20S with 3X-FLAG has no effect on cytosolic proteasomes measured by proteasome assembly, activity, and concordantly, no obvious effects on cell health (**Fig 1B,C**). We fail to detect FLAG expression in the livers from 20S-FLAG/Baf53b-Cre mice nor can we affinity isolate proteasomes using the FLAG epitope handle from the liver, indicative of the selective and inducible nature of our desired transgene (**Fig S1C, D**). We find that neuronally expressed 20S-FLAG/Baf53b-Cre mice appear indistinguishable from their wild-type littermates, supporting the conclusion that 20S-FLAG proteasomes are inert and do not disrupt native proteasome function.

To test whether the 20S-FLAG was efficiently incorporated into the plasma-membrane-bound 20S NMP, we performed surface biotinylation experiments out of both neurons and hippocampal tissue from 20S-FLAG transgenic mice. Hippocampi from 20S-FLAG/Baf53b-Cre mice were

incubated with a cell-impermeable sulfonylated Biotin-NHS-Ester to label surface-exposed amines and surface proteins were pulled down on streptavidin beads. We observe strong FLAG expression in the surface fraction, indicating that the FLAG tag is incorporated into the NMP (**Fig 1D**). We fail to observe this in 20S-FLAG mice without Cre (**Fig 1D**). By blotting using an antibody which detects 6 of the 7 alpha subunits of the 20S proteasome, we can clearly distinguish the modified Psma3 subunit overlaying with the FLAG signal, denoting modification of the endogenous protein (**Fig 1D**). To test if our transgenic system is functional in primary cultures, we performed postnatal dissections and grew primary cortical neuronal cultures from 20S-FLAG mice. Transgene expression was induced by transducing days in vitro (DIV) 2 cultures with AAVs to express Cre recombinase and we performed surface biotinylation experiments at DIV14 (**Fig S1E**). We did not detect FLAG without AAVs to express Cre, once again supporting the claim that our transgene is not leaky. Notably, we find that homozygote compared to heterozygote littermates express identical total levels of the FLAG-tagged subunits, but a two-fold increase of FLAG tag which is surface-exposed (**Fig S1F**). These data are consistent with only one of the symmetric ends of the 20S being exposed to the extracellular space, which is consistent with our hypothesis and model that the membrane topology of the NMP spans the membrane.

Next, we purified the FLAG-tagged NMPs to determine their composition. Affinity isolation of NMP complexes was done by first purifying plasma membrane preparations from 20S-FLAG/Baf53b-Cre brains, extensive washing with low concentrations of detergent to remove cytosolic proteins, and then a high detergent extraction. To validate our purification protocol, we immunoblotted our membrane preparations to monitor for cytosolic contamination. We find our membrane preparations were enriched in membrane proteins such as the GluR1 subunit of the glutamate receptor and depleted of cytosolic proteins like Actin (**Fig S1G**). Identical samples were prepared from the cytosol. Affinity isolated NMPs and cytosolic proteasomes were subjected to mass spectrometry analysis. As expected, we find common signatures of 20S subunits between both cytosolic proteasomes and NMPs and a significant depletion of 19S subunits in the NMP isolations. We identified 86 proteins enriched in the NMP isolations which are depleted in the cytosolic fraction. This revealed significant enrichment of the GPM6 glycoprotein which we previously described[3] (**Fig 1E**). The majority of the other components identified are involved in synaptic vesicle recycling and membrane trafficking (NSF, Clathrin, Dynamin, COPI, Vps35 and Sorl1, AP2 and AP3). We believe this reflects the underlying cellular mechanisms for regulating localization of these complexes to the plasma membrane. Standing out against this common theme of synaptic and membrane-recycling proteins, we found a surprising and strong enrichment of ApoE and the ApoE receptor Lrp1 (**Figure 1E, Supplemental Table 1**). We first validated these proteomic data by affinity isolating FLAG-NMPs as well as cytosolic FLAG-proteasomes and then immunoblotting these samples with antibodies against ApoE and Lrp1, as well as antibodies against 19S and 20S subunit components. We find enrichment of FLAG and 20S proteasome subunits in affinity isolations

from the membrane fraction and a lack of 19S subunits. Here, we validate our proteomic data by also identifying robust co-purification of ApoE and Lrp1 with the FLAG-NMP (**Fig 1F**).

ApoE isoforms differentially modulate NMP surface localization *in vivo*

To test whether the ApoE/Lrp1 interaction with NMPs may be functionally relevant, we used the well-established Lrp1 receptor antagonist Receptor-associated protein (RAP) which induces Lrp1 internalization[30-32]. We used a stable variant of RAP which contains a stabilizing mutation to protects against pH-induced denaturation and maintains a higher percentage of internalized Lrp1[30]. After purifying RAP, we incubated primary neurons with RAP and measured NMP levels using surface biotinylation. We find that RAP rapidly decreases the surface expression of Lrp1, as expected (**Fig 2A**). We also find that RAP reduces surface localization of NMPs, measured by surface β5 signal (**Fig 2A**). We fail to detect intracellular labeling measured by a lack of actin in our streptavidin surface pulldowns, validating our surface biotinylation protocol. These data served as the first demonstrate that the ApoE receptor Lrp1 which co-purified with NMPs can regulate NMP localization. This finding served as the impetus to determine whether ApoE could also influence NMP localization.

ApoE can be expressed as one of three isoforms in human: ApoE4, ApoE3, and ApoE2, each of which differs by only two residues. Despite this seemingly small difference, ApoE4 confers a significant increase in the propensity to develop Alzheimer's Disease while ApoE2 confers a protective effect against AD. Given that we find ApoE co-purifies with the NMP, we wanted to test the hypothesis that ApoE isoforms can modulate NMP localization and function. To test this hypothesis, we obtained human ApoE isoform knock-in (KI) mice, where the endogenous mouse APOE gene is replaced with a cassette encoding the human APOE gene[33]. These mice therefore only express either the ApoE2, ApoE3, or ApoE4 isoforms. ApoE-KI mice were perfused and then hippocampus and primary motor cortex were microdissected and subjected to surface biotinylation. Biotinylated proteins were pulled down and immunoblotted to reveal surface protein localization. We measured NMP localization to the plasma membrane by immunoblotting against the 20S proteasome subunit β5. We found a strong reduction of NMP localization to the plasma membrane in the hippocampus from ApoE4-KI mice, compared to ApoE3-KI or ApoE2-KIs (**Fig 2B**). We observe a significant difference between ApoE3 male and female mice, where female ApoE3 mice have 50% fewer surface-localized NMPs than male ApoE3 mice in hippocampus (**Fig 2B**). We find this noteworthy in the context of the extensive literature on the influence of biological sex on AD pathogenesis[24,34-37]. We find coordinate changes in Lrp1, but fail to detect any change in a membrane-loading control such as the transferrin receptor (TFR) which should be unaffected by ApoE. When we monitor NMP localization in the primary motor cortex from the ApoE-KI mice, we find that NMP surface localization in ApoE4-KIs is reduced compared to ApoE2-KIs and we observe a trend, but no significant change in ApoE4-KI compared to ApoE3-KI (**Fig S2A**). These data may be

attributable to differences in ApoE expression in different brain regions[33], a dimension which we have not systematically investigated.

Given the complexities of region-specific ApoE isoform expression *in vivo*, we approached the effect of ApoE isoforms in a more defined and tractable primary neuronal culture system. This approach would also allow us to define when ApoE isoforms are introduced as a means of temporal control. We generated postnatal primary cortical neurons from either 20S-FLAG transgenic animals or primary embryonic cortical neurons from WT animals and conducted imaging and biochemical experiments to measure NMP localization. ApoE is a lipoprotein, and in the brain is largely thought to be released by glia in the lipid-bound form[24,38]. Therefore, for our experiments in primary neurons we tested whether or not the lipidation of ApoE would also influence NMP localization. We purified lipidated recombinant ApoE isoforms, referred to as POPC/Cholesterol (PC)-ApoE2, E3, and E4. These lipoparticles were validated by SEC and negative stain EM (**Fig S2B**) and have been demonstrated to resemble the endogenous ApoE lipoparticles observed in the brain[39]. We incubated DIV14 primary neurons from 20S-FLAG transgenic mice with delipidated and PC-ApoE for 24 hours and then performed surface biotinylation experiments. Lysates were pulled down on streptavidin beads and immunoblotted for FLAG and 20S proteasome subunits to measure NMP surface localization. We find that PC-ApoE, and not the delipidated versions, modify NMP surface localization with the rank order PC-ApoE4<Vehicle,E3<E2 (**Fig 2C**). We fail to detect cytosolic proteins such as the 19S cap or actin and find no change in other membrane proteins such as GluN1, suggestive of no global change in membrane protein internalization or degradation. The isoform-dependent effect on NMP localization is also likely driven by ApoE itself, as the addition of just the liposomes without ApoE does not modify NMP localization (**Fig 2C**). We find identical results in primary WT neurons, suggesting that the observed ApoE-isoform dependent effect on localization are not an artifact of the FLAG epitope tag on NMPs (**Fig S2C**).

FLAG-NMPs are a useful tool to measure the surface localization of NMPs and we next took advantage of the epitope tag to test whether ApoE isoforms modified the subcellular distribution and localization of NMPs in intact neurons. We used antibody feeding onto live neuronal cultures from the 20S-FLAG mice transduced with AAVs to express Cre[40,41]. No staining was observed using secondary alone controls (**Fig S2D**) or when feeding an antibody against intracellular protein MAP2 (**Fig S2E**). After live cell anti-FLAG antibody feeding, neurons were fixed, permeabilized, and stained for total intracellular MAP2 to label dendrites. Consistent with this approach being a robust measure of NMP localization, we observed punctal NMP localization when feeding anti-FLAG antibodies, of which more than 90% was within 2 μm of the MAP2 signal. We observe significant overlap of surface FLAG signal with MAP2-positive protrusions that resemble dendritic spines (**Fig 2D**). We observe that lipidated ApoE2 particles increase NMP surface localization by nearly twofold and that lipidated ApoE4 particles reduce NMP surface localization by nearly threefold compared to PC vehicle or ApoE3 particles (**Fig**

2D). In total, these data recapitulate the observations from the ApoE-KI mice and support our hypothesis that extracellular ApoE isoforms can influence NMP localization and function in a manner consistent with the risk they pose for Alzheimer's Disease.

NMP localization is reduced in vulnerable brain regions in the human brain and is further reduced by ApoE4 genotype

We next tested whether ApoE-dependent localization of NMPs is observable in postmortem patient tissues. For these analyses, we studied a cohort of 18 individuals (14 ApoE3/3 and 4 ApoE4/4) from the Massachusetts General Hospital Brain Bank. The ApoE3/3 subgroup was subdivided into 5 negative diagnoses and 9 positive diagnoses for AD. Sex was evenly distributed in samples except for the ApoE4 cases which were all male. This design allows us to compare the effect of AD on NMP localization, regardless of ApoE genotype, as well as the effect of ApoE genotype on NMP localization. We obtained material from the Brodmann Area (BA4 - primary motor area) and BA7 (parietal associative area). We analyzed these regions as a means of untangling how NMP localization changes in pathologically affected (BA7) versus unaffected (BA4) regions of the brain. We fractionated these samples to remove nuclei, mitochondria, and cytosol, enriching for plasma membranes and detergent-insoluble proteins. Human tissues required stringent wash steps to remove cytoplasmic contamination – we monitored this using LLVY-based proteasome activity assays out of the supernatant of our washes and continued washing our plasma membrane preparations until cytosolic proteasome contamination was undetectable (**Fig 3A**). Many previously reported plasma membrane preparations remove NMPs or do not keep NMPs intact. Therefore, we used a synthetic digitonin substitute glyco-diosgenin (GDN) which maintains NMP associations of NMPs with plasma membrane for our wash and extraction conditions.

We then subjected isolated plasma membranes to quantitative TMT proteomics analysis. TMT proteomics enables unbiased quantification of the proteome and the ability to make quantitative comparison across samples. Since AD-affected regions generally have fewer healthy cells and are dying, we compensated for this by first normalizing protein loading into the mass spectrometer and second, normalizing the data against the total TMT signal per channel which accounts for protein abundance. Given the number of samples, we combined two TMT 16-plex experiments with a shared internal standard which enabled quantitation across TMT experiments. These data validate our plasma membrane enrichment protocol – we find a significant enrichment for membrane-bound and membrane-associated proteins and a strong depletion of cytosolic proteins, including the 19S cap (**Supplemental table 2**). Consistent with previous global proteomic analysis from AD brains, we find a significant increase of C4b[42], AnxA1[43], Gpnmb[44], and Tau (Mapt)[45] in AD brains compared to unaffected controls (**Fig 3B**). We also find a significant decrease in Vgf[46] and Slc30A3[47] consistent with previous AD global proteomic datasets (**Fig 3B**). We expect to find aggregated proteins in this protocol since our plasma

membrane enrichment method would also isolate large aggregates such as aggregated Tau in the AD brain.

After validating our approach, we next analyzed the effect of AD on NMP localization, measured by the relative quantity of 20S proteasome subunits in our quantitative mass spectrometry dataset. First, in comparing AD samples to cognitively normal controls, we find a striking reduction in nearly every 20S proteasome subunit in the plasma membrane fraction from BA7 tissue – a brain region susceptible to neurodegeneration in AD (**Fig 3B, Supplemental table 2**). We next sought to determine whether ApoE genotype influenced NMP localization in human tissue. Given the significant effect of AD on NMP localization, we constrained the analysis of the effect of ApoE genotype on NMP localization. We observe a clear trend of reduced 20S proteasome subunits in the membrane fraction in the ApoE4 genotype compared to ApoE3 genotype in the BA7 vulnerable brain region (**Fig 3C**). However, AD pathology exerts a strong effect on the proteome and on NMP localization, making it more difficult to isolate the specific effects of ApoE isoforms on NMP localization in human samples.

To circumvent this issue, we instead looked for changes in the surface localization of NMPs by immunoblot analysis measured by β5 expression in the membrane-enriched fraction. We control for sample loading by normalizing against Kv1.2, a protein whose expression has been reproducibly demonstrated as unchanged in the AD brain[48]. First, we validate our proteomics data and find a twofold reduction of NMP surface expression in AD patients compared to controls in the BA7 region (**Fig 3D**). Moreover, we find a statistically significant reduction in NMP localization from ApoE4/4 tissue compared to ApoE3/3 tissue, even when adjusted for AD (**Fig 3D**). We find concordant changes in Lrp1, consistent with our model that NMPs and Lrp1 respond together in response to ApoE isoforms. We find no changes in the total expression of the 20S proteasome from the cytosolic fraction, suggesting that the changes we observe are specific to NMP localization and not a global change in proteasome levels. Consistent with these observations, using LLVY degradation experiments to measure the catalytic activity of the proteasome, we found a significant reduction in NMP activity in AD samples compared to unaffected controls and no change in cytosolic proteasome activity (**Fig S3**).

Next, we turned our attention to the BA4 region – a region where AD pathology should be relatively minimal. Here, unlike BA7, we find similar surface localization of NMPs between patients with and without AD. However, once stratified by ApoE genotype, we find that ApoE4/4 patients have a nearly 50% reduction in surface localization of NMPs compared with ApoE3/3 patients (**Fig 3E**). This demonstrates that ApoE4 can influence NMP localization in the absence of AD pathology, providing clear demonstration that ApoE genotype modulates NMP localization in humans. Together, we make two conclusions based on these data: 1) that NMP localization is reduced in brain regions which have increased susceptibility to AD pathology and 2) that ApoE4 reduces NMP localization potentially broadly compared to ApoE3. These data

suggest that a reduction in NMP localization, either through ApoE4 or other unidentified mechanisms, are correlated with AD pathology and susceptibility.

Quantitative proteomics reveals that selective inhibition of NMPs induces Tau aggregation

What is the consequence of ApoE4-dependent reduction in NMP function, or more broadly, any reduction in NMP function? Predicated on the principle that NMPs are complexes which degrade protein substrates, we considered that one testable consequence of reduced NMP function would be an accumulation of substrates. However, in order to test this hypothesis, we required an NMP-specific inhibitor. We previously accomplished this by biotinylating the N-terminus of Epoxomicin, a covalent and highly selective inhibitor which exclusively targets the catalytic β subunits of the proteasome, with no off-target reactivity[49-52]. We previously found that this small modification rendered epoxomicin cell-impermeable for up to an hour[4]. While this approach was useful for identifying rapid activity-dependent substrate degradation and general principles of NMP-mediated degradation, one hour is too little time to identify the consequences of NMP inhibition without driving neuronal activity.

Based on principles of drug design, we considered that introducing a longer PEG linker between the N-terminus of Epoxomicin and biotin would decrease the permeability of biotin-epoxomicin and allow us to reveal the long-term consequences of NMP inhibition[53,54]. We synthesized click-able analogs of Epoxomicin (Azide-Epoxomicin) that would allow us to add a broad range of linkers (**Fig 4A**). Modification of the non-reactive end of epoxomicin has been shown not to change the selectivity of Epoxomicin for the proteasome[51,55,56].We then conjugated Biotin-PEG24-Alkyne to Epoxomicin, producing Biotin-PEG24-Epoxomicin, or iBEp (**Fig 4A**). We observe efficient conjugation by HPLC analysis (**Fig S4A, B, C, D**). All molecules were HPLC-purified as single peaks and confirmed by LC/MS analysis (**Fig S4D, E**). Because epoxomicin covalently and irreversibly binds the catalytic β subunits of the proteasome, the biotin moiety on iBEp also serves as a tracer to identify which proteasomes are inhibited by monitoring biotin signal on an SDS-PAGE gel[51,55,56]. To test the permeability of our compounds, we incubated primary cortical neurons with iBEp over a time course and prepared both cytosolic and plasma membrane-enriched fractions. Samples were immunoblotted and probed for cytosolic marker Actin and membrane protein GluR1 to validate our fractionation (**Fig 4B**). We found specific biotin signal corresponding to covalent inhibition of the proteasome only in the membrane fraction, and not in the cytosol, over a 24 hour incubation in primary neurons (**Fig 4B**). We find significant covalent modification of NMPs despite the small loss of efficacy of iBEp compared to Epoxomicin as a consequence of the long PEG linker (**Fig S4F**). As an orthogonal measure of cell penetrance, we tested whether cytosolic proteasomes were affected by iBEp treatment. We subjected cytosolic and membrane fractions from iBEp-treated neurons to LLVY-based proteasome activity assays. Cytosolic proteasome activity remains completely intact from iBep-

treated neurons compared to DMSO controls, but proteasome activity in the membrane fraction is almost entirely abrogated (**Fig 4C**). This suggests that NMPs are completely inhibited following iBEp incubation but cytosolic proteasomes remain unaffected.

We also wanted a cellular functional readout of whether our cell-impermeant inhibitors affected cytosolic proteasomes. One of the most penetrant and robust consequences of total proteasome inhibition is the induction of autophagy as a cellular response mechanism to counteract the lack of proteasomal degradation. To test this, we assayed three autophagy markers, p62 levels, LC3bI/II ratios, and Ulk1 levels. Each are robust markers of different steps of autophagy. p62 has been demonstrated to be rapidly induced upon proteasome inhibition and LC3bI/II induction is thought to be slower, while Ulk1 is important for early phagosome formation[57]. Cytosolic proteasome inhibition has been reproducibly demonstrated to induce a strong increase in p62 levels in neurons[19,20,22,57]. Consistent with these reported observations, we find a strong induction of p62 levels and little to no change in LC3bI/II following 12 hours of total proteasome inhibition with epoxomicin (**Fig 4D**). However, when we treat primary neurons with iBEp, we observe no change in either p62 or LC3bI/II levels (**Fig 4D**). These data are a functional demonstration that iBEp is cell-impermeable to neurons.

Leveraging this tool, we incubated DIV12-14 primary cortical neurons with cell-impermeable proteasome inhibitors in biological duplicate for 1 and 6 hours, prepared sarkosyl-soluble and sarkosyl-insoluble samples, and then collected and processed samples for quantitative TMT-based proteomics (**Fig 4E**). We analyzed proteins which increase over the time-course in the soluble fraction. First, we recapitulate our previously published data and find that NMP inhibition induces the accumulation of previously reported substrates such as Rgs4, c-Fos, Sox4, Snurf, Arc, and Bex2 in the soluble fraction (**Fig 4F, G, Table S3**)[4]. Importantly, we also do not see accumulation of known ubiquitin-dependent substrates such as PSD-95, Homer1, or GKAP[58-60] (**Fig 4G**). We also fail to observe an increase in p62, LC3b, GabarapL1, or any other marker of autophagy[1,61] (**Fig 4G**). This provides orthogonal evidence that these compounds do not detectably penetrate cells and demonstrates the validity of this approach to determine the consequences of selective NMP inhibition. These validate our previous data identifying NMP substrates and extend them by demonstrating NMP-dependent substrate turnover in a context without modulating neuronal activity and over extended periods of time.

Turning to the insoluble fractions, our quantitative proteomic analysis revealed a selective pattern of protein aggregation following NMP inhibition. We find that only 52 proteins are aggregated in response to NMP inhibition (**Fig 4H**), in contrast with over 250 proteins increasing in the soluble fraction (**Fig 4F**). We observe interesting changes, such as the aggregation of small heat shock proteins (Hspb1 and Cryab) and RNA-binding proteins such as Fus (**Fig 4H**). To narrow in on this list and identify specific targets that aggregate following NMP inhibition, we quantitated which proteins changed in the insoluble fraction, but showed no change in the

soluble fraction (**Fig 4I**). This analysis identified only four proteins which show a specific increase in the insoluble fraction relative to the soluble fraction (Cmkt1, Tau, Taf15, and Hspb1) and one protein which increases in the soluble fraction and showed no change in the insoluble fraction (Plk2) (**Fig 4I**). Of note, Taf15 has previously been observed in detergent-insoluble fractions of brains from Alzheimer's patients, correlated with both Amyloid β and Tau insolubility[62-65]. This highly specific induction of Tau aggregation following NMP inhibition, taken together with our data that the ApoE4 AD risk variant reduces NMP localization and function, places NMPs at the crux of protein aggregation in AD.

NMPs are licensed to degrade newly synthesized endogenous Tau in vitro and in vivo

We specifically wanted to validate our finding that Tau aggregates in response to NMP inhibition. We chose to study the turnover and degradation of endogenous murine Tau and human Tau without pathogenic aggregation-driving mutations in Tau. This approach allowed us to more carefully dissect the precise roles for NMPs in Tau regulation. We therefore cultured primary mouse cortical neurons from either embryonic WT C57/B6 mice or from postnatal hTau-KI mice, where the entire mouse MAPT sequence was replaced with the human MAPT sequence at the endogenous locus[66]. hTau-KI mice express all of the isoforms of normal human Tau protein using the endogenous MAPT regulatory elements and therefore, hTau is expressed at normal physiological levels. DIV12-14 neurons were treated with either the NMP inhibitor iBEp or the total (NMP and cytosolic) proteasome inhibitor Epoxomicin. We then performed sarkosyl fractionations to separate treated neurons into soluble and insoluble fractions and immunoblotted these fractions for Tau and GAPDH. We observed no Tau signal in identical experiments in primary neurons cultured from Tau-KO mice, demonstrating the specificity of our antibodies and approach (**Fig S5A**)[67]. The R2295 antibody reacts against both human and mouse Tau isoforms and is highly specific, making it the ideal tool to monitor endogenous Tau turnover in WT and hTau-KI samples. We found a significant increase in sarkosyl-insoluble Tau from both the WT (**Fig 5A**) and hTau-KI neurons treated with iBEp (**Fig 5B**). Intriguingly, we find no change in Tau aggregation in neurons treated with the cell-permeable Epoxomicin, despite the fact that Epoxomicin inhibits cytosolic proteasomes and NMPs (**Fig 5 A,B**). We reason that initially, Epoxomicin inhibits NMPs and induces Tau aggregates, but we cannot detect them because simultaneous inhibition of cytosolic proteasomes induces autophagy and other compensatory mechanisms which can clear aggregates. This claim is supported by an extensive body of work on Tau clearance mechanisms[19-23,57]. We posit that such compensatory mechanisms are not triggered when NMPs are specifically inhibited, which is consistent with our observations that Epoxomicin induces p62 expression whereas iBEp does not (**Fig 4D, G**). These data demonstrate the importance of specifically distinguishing the function of NMPs separately from that of cytosolic proteasomes. Notably, we conclude that NMP-specific inhibition induces the aggregation of Tau, placing NMPs as a pivotal mechanism in determining aggregate formation instead of the canonical role of proteasomes in protein clearance.

There are many possible mechanisms for how NMP inhibition could induce Tau aggregation. NMPs are 20S complexes and do not have the machinery to recognize ubiquitin or unfold substrates[3,4]. Instead, NMPs are thought to co- or peri-translationally degrade substrates and do not degrade substrates which are fully folded[4]. Therefore, we next tested whether Tau degraded by NMPs was newly synthesized. We reasoned that if we observed Tau aggregation while both NMPs and protein synthesis was inhibited, then the effect of NMP inhibition on Tau would likely be through a secondary or tertiary mechanism (**Fig 5C**). We incubated primary neuronal cultures with either iBEp or Epoxomicin and then co-incubated these cultures with Cycloheximide, which blocks translation elongation. Here, we reproduce the iBEp-induced Tau aggregation and find that cycloheximide blocks this iBEp-mediated increase in both hTau-KI primary neurons (**Fig 5D**) and in WT primary neurons (**Fig S5B**). These data suggest that NMPs degrade specifically newly synthesized Tau. While this does not preclude secondary intermediate mechanisms, we suggest that inhibition of NMPs with iBEp induces Tau aggregation because newly synthesized Tau is a direct substrate of NMPs.

Many of our experiments rely on the use of iBEp, because the biotin tracer on a covalent and specific inhibitor allows us to track which proteasomes are inhibited. However, we wanted to validate our findings using a proteasome inhibitor with a distinct mechanism of action from Epoxomicin. We therefore modified MG132, a reversible peptide aldehyde proteasome inhibitor, with a sulfonated biotin linker on the nonreactive N-terminus[52]. This negatively charged water-soluble linker renders Sulfo-MG132 cell-impermeable, much like the historical use of sulfonated linkers to perform surface biotinylation (**Fig 5E).** We observe efficient conjugation by HPLC analysis (**Fig S5C, D**). All molecules were HPLC-purified as single peaks and confirmed by LC/MS analysis (**Fig S5E, F**). We find significant inhibition of proteasomes using Sulfo-MG132 despite the small loss of efficacy of Sulfo-MG132 compared to MG132 as a consequence of the linker (**Fig S5G**). MG132 is a reversible inhibitor and therefore, we cannot detect the covalent modification of the proteasome subunits. Instead, we turned to cellular and functional readouts of permeability. We found a similar induction of autophagy markers in neurons treated with MG132 as with epoxomicin and a similar lack of induction with Sulfo-MG132 as with iBEp (**Fig 5E)**. Confident in its use as a cell-impermeable inhibitor, we next incubated DIV14 primary hTau-KI neurons with Sulfo-MG132, with or without cycloheximide. We find that Sulfo-MG132 induces similar aggregation of hTau into the sarkosyl-insoluble fraction as iBEp (**Fig 5F**). Moreover, we find that MG132, like Epoxomicin, does not affect the aggregation of Tau. Finally, we find that cycloheximide also blocks the effect of sulfo-MG132 on Tau aggregation, consistent with our previous observations using iBEp (**Fig 5F**).

Next, we examined whether NMP inhibition would induce Tau aggregation *in vivo*. We tested iBEp permeability *in vivo* by stereotactically injecting iBEp into the mouse hippocampus for at least 72 hours. Hippocampi were microdissected and separated into cytosolic and membrane-enriched fractions and samples were immunoblotted (**Fig 5G**). We fail to observe penetration

into the cytosol until we inject 64μM, so we chose to inject at 10-fold under this dose as a starting concentration (**Fig 5G**). We performed stereotactic injections of iBEp and contralateral injections of PBS into the hippocampus of WT, hTau-KI, and Tau-KO mice. After 72 hours, we collected the hippocampi and performed Sarkosyl extractions into soluble and insoluble fractions. We fail to observe any detectable Tau in the Tau-KO mice in PBS or iBEp-injected hippocampi (**Fig S5H**). Mirroring our data in primary neurons, we find a strong increase of sarkosyl-insoluble Tau in hippocampi from hTau-KI mice injected with iBEp (**Fig 5H**). in the propensity for Tau to aggregate following NMP inhibition. While there does seem to be a trend that female mice accumulate more Tau in response to NMP inhibition than male mice, we find no statistically significant sex differences. However, this statement is caveated by the fact that these experiments are too underpowered to determine the influence of sex on NMP inhibition-induced aggregation. Next, we tested whether inhibition of protein synthesis blocks the aggregation of Tau. We co-injected cycloheximide and iBEp together contralateral to iBEp alone. Here, we find a dramatic reduction of Tau aggregation in the hippocampus after co-incubation of iBEp with cycloheximide compared to iBEp alone (**Fig 5I**). This extends the phenomenon we observed *in vitro* and provide the first ever demonstration of NMP-dependent substrate degradation *in vivo*. These data are also the first demonstration that *in vivo* NMP inhibition results in protein aggregation. Taken together, using two chemically distinct cell-impermeable inhibitors, we conclude that inhibition of the NMP induces Tau aggregation and that newly synthesized Tau is uniquely susceptible to NMP-mediated degradation.

NMP complexes determine the ApoE-isoform dependent risk for Tau aggregation and pathology in vivo

In addition to Tau aggregation, another hallmark phenotype of AD and other neurodegenerative disorders is Tau hyperphosphorylation[68,69]. We noticed that NMP inhibition induces the shift of sarkosyl-insoluble Tau into a species which migrates at a higher molecular weight on an SDS-PAGE gel. Similar shifts in molecular weight of Tau are observed in Paired Helical Filaments from the AD brain. These can in part be due to Tau phosphorylation at many residues. Therefore, we next wanted to address whether iBEp-induced Tau aggregates are also phosphorylated. We treated primary WT neurons with iBEp for either 1, 6, or 24 hours and then performed sarkosyl fractionations. Soluble and insoluble fractions were processed for TMT labelling in preparation for quantitative mass spectrometry and then peptides were run over an Fe-NTA column to enrich for phospho-peptides (**Fig 6A**). We then used this enriched population for quantitative phospho-proteomics analysis (**Table S4**). Here, we find a time-dependent increase in Tau phosphorylation at only 4 of 26 identified sites which correspond to human S202, T205, T217, and S404 (**Fig 6A**). This is a remarkably specific signature of phosphorylation which corresponds to sites at which Tau is phosphorylated in the AD brain (S202 – CP13[70], T205 – AT8[71], and S404-PHF1[72]) as well as CSF biomarkers for AD progression (T217)[73]. To validate these data, we treated hTau-KI neurons with iBEp and then fixed and stained these neurons. We observed no staining in neurons cultured from Tau KO mice using the R2295 antibody to detect total Tau or the CP13

antibody to detect S202 (**Fig S6A**). However, we could not use the AT8 antibody for immunocytochemistry (ICC) because we found extensive non-specific staining in the Tau KO controls (**Fig S6A**). Incubating neurons with secondary antibodies alone showed no signal (**Fig S6B**). We therefore exclusively used CP13 for our ICC experiments. We find a significant elevation of CP13 signal in iBEp-treated primary hippocampal hTau-KI neurons compared to controls (**Fig 6B**). To validate these data, we conducted immunohistochemical (IHC) analysis of sections from hTau-KI mice where we had stereotactically injected iBEp and PBS contralaterally. After stereotactic injections, animals were allowed to recover for 72 hours and then were perfused and sectioned for IHC. We observed no staining in the Tau KO mice using the AT8 antibody or with secondary antibodies alone (**Supp Fig S6C**, **S6D**). We observe a threefold induction of phosphorylated Tau signal in hippocampi injected with iBEp compared to the contralateral PBS controls. We see strong accumulation of phosphorylated, and presumably aggregated, AT8+ Tau into the stratum radiatum and stratum moleculare (**Fig 6C**). We find this staining mislocalized to somatodendritic compartments in the contralateral iBEp-injected hemisphere. Surprisingly, we find a complete abrogation of this accumulation when we co-inject cycloheximide and iBEp in the ipsilateral hemisphere compared to the contralateral injection of iBEp alone (**Fig 6C**). This extends our *in vitro* data to demonstrate that NMP inhibition induces aggregation of pathological Tau *in vivo* and suggests that Tau aggregates that form as a result of NMP inhibition are composed of newly synthesized Tau.

Our overall hypothesis is that ApoE regulates NMP localization and function, in the rank order ApoE4<E3<E2, and that specific inhibition of NMPs induces the aggregation of newly synthesized Tau. Given the evidence that NMPs are integral to regulating Tau aggregation, we predicted that neurons from ApoE4-KI mice would be more susceptible to Tau aggregation relative to neurons from ApoE3-KI or E2-KI mice. To test this prediction, we crossed each of the ApoE-KI lines to the hTau-KI lines, generating mice which endogenously express ApoE2, E3, or E4 as well as hTau. DIV14 primary neurons from each line (E2/hTau double KI, E3/hTau double KI, and E4/hTau double KI) were then treated with a range of iBEp doses spanning four log units. Neurons were then separated into sarkosyl-soluble and insoluble fractions and immunoblotted. We found that neurons from each line had no Tau aggregates at baseline, which suggests that the reduced levels of NMPs in the E4-KI mice is not in-and-of-itself sufficient to drive Tau aggregation (**Fig 6D**). However, after treatment with even the lowest dose of iBEp, we found accumulation of sarkosyl-insoluble Tau in E4-KI neurons, rendering E4-KI neurons over 50-fold more susceptible to Tau aggregation than E3-KI neurons (**Fig 6D**). Conversely, neurons from E2-KI mice were 5-fold less susceptible to NMP-inhibition induced Tau aggregation (**Fig 6D**). Overall, these data demonstrate that ApoE isoforms differentially shift the threshold for NMP-dependent Tau aggregation in a manner concordant with the risk they pose for AD (E4>E3>E2).

Discussion

Many studies have demonstrated the importance for proteasome-related factors, such as ubiquitin ligases[74,75], trafficking[76], and kinases[77,78] as changing or relevant to neurodegeneration. However, to our knowledge, this study represents the most direct connection yet between the proteasome to the genetics and epidemiology of AD by showing that NMPs co-purify with ApoE and are influenced directly by ApoE isoforms in a manner consistent with the risk that ApoE isoforms pose for AD. Moreover, this represents the first demonstration that the failure of a proteasome system in neurons, the NMP, directly induces and is sufficient for Tau aggregation and pathology in vivo. In doing so, the NMP links ApoE isoform-dependent risk for AD directly with a new mechanism for Tau turnover and aggregation.

The conventional thinking around proteasomal degradation is that proteasomes are largely the executors of the combined actions of ubiquitin ligases, deubiquitinases, and proteasome shuttling factors[79,80]. NMPs, by degrading newly synthesized proteins co- or peri-translationally, are positioned to bypass these canonical mechanisms. Our study highlights the NMP as a proteasome complex that directly influences protein aggregation. Furthermore, we suggest that NMP localization and function itself is a determinant for the proteostatic capacity of neurons to defend against Tau aggregation and proteostasis dysfunction broadly.

To test the role for proteasomes in any physiology, the gold standard experiments are to either interfere with the factors important for substrate ubiquitylation and delivery[81] or to impinge on the proteasome itself using inhibitors[49,82]. Such studies have not been able to determine the sole action of NMPs or cytosolic proteasomes because of compensatory responses by autophagy or the proteasome bounce-back response. By synthesizing cell-impermeable inhibitors that selectively block NMPs and not the cytosolic proteasome, we have been able to discriminate a few unique properties of NMPs in this study. For example, we were able to shed light on the controversy of whether and how proteasomes in neurons degrade Tau. We anticipate that these inhibitors, and the tools we have built to visualize and purify NMPs, will enable the broad study of NMPs in various aspects of neuronal physiology and pathophysiology.

We demonstrate that ApoE co-purifies with the NMP and that ApoE isoforms can differentially modulate the localization of NMPs to the plasma membrane. The mechanisms by which ApoE influences NMP localization remain unexplored in this study. ApoE is found as a lipoparticle and the classic role for ApoE is a cholesterol carrier[83]. While we demonstrate only lipidated ApoE can influence NMP localization, we do not understand whether the lipids transported by ApoE are involved in regulating NMPs or if simply the lipidated molecules are more efficiently able to interact with the NMP complex. ApoE isoforms influence NMP localization to different magnitudes in different brain regions, where more vulnerable regions are more susceptible to neurodegeneration. We speculate this may be due to a simple explanation like differential ApoE

expression in different brain regions, or more interestingly, unique cell-type-specific mechanisms which transduce the ApoE isoform to induce the specific change in NMP localization

NMP dysfunction can directly induce Tau aggregates in neurons, without the need for pathogenic mutations. We suggest that this may be important for Tau aggregation observed in a high percentage of sporadic AD patients who do not contain genetic lesions in the Mapt locus. We find NMPs are licensed to degrade newly synthesized Tau and that that newly synthesized Tau is uniquely susceptible to aggregation and pathology. One implication of our model is that targeting phosphorylated or already aggregated Tau may not be sufficient to completely clear pathogenic Tau, since NMP dysfunction will continue to feed more Tau into aggregates. By showing that NMP inhibition does not induce autophagy, we show that NMP inhibition is not recognized by canonical stress responses and may bypass other protein quality control pathways. This makes NMP inhibition potentially particularly deleterious to neurons. We find it noteworthy that neuronal activity has been reported to be involved in the pathogenesis and aggregation of Tau in the context that NMP-dependent degradation is regulated by neuronal activity. Along these lines, Tau has also been shown to be released by neurons to regulate intracellular spread[84,85]. Whether NMP inhibition modulates the release of extracellular Tau will be an interesting question moving forward, given we observe an NMP-inhibition induced increase of the phosphopeptide which correlates with increase extracellular Tau burden.

The relevance for NMPs in other aspects of neurodegeneration will be critical to explore. For example, given we observe NMPs at synapses and that AD is characterized by a loss of synapses, we wonder if NMP dysfunction could induce synaptic dysfunction. In a similar vein, ApoE is intricately linked with the production and clearance of amyloid β[86] and whether NMP inhibition induces changes in amyloid processing or amyloid β production would be worth investigating.

This study is the first to demonstrate that NMPs could play important roles in the biology underlying neurodegenerative diseases. As a concluding note, our findings only increase the urgency to understand fundamental aspects of NMP biology. For example, revealing the genetic and cell biological elements which control NMP localization and trafficking are likely to be critical to reveal how ApoE exerts an effect on NMP localization. The other factors that we identify that co-purify with NMP suggest the importance of synaptic vesicle trafficking and other membrane trafficking mechanisms. Understanding these, as well as related mechanisms like how only newly synthesized proteins are degraded by NMPs, are likely to open up therapeutic avenues that can impinge on NMP biology to boost proteostasis and delay or prevent aggregation.

Acknowledgements

We thank the families and patients who contributed human tissue which enabled the discoveries in this manuscript. We thank Virginia Lee for the R2295 antibody. We also thank Abid Hussaini for providing the hTau-KI mice and Carol Troy for the perfusion setup Claire Chen for IHC training. We thank Ulrich Hengst, Clarissa Waites, and Alfred Goldberg for invaluable discussions and Sadie for invaluable laboratory support. We also thank Michael Shelanski, Richard Mayeux, and the Taub Institute for support and start-up funding.

Funding Sources

KVR supported by NIH Director's Early Independence Award DP5OD028133, Department of Defense CDMRP award W81XWH-21-1-0093, Fidelity Biomedical Research Initiative, Norm Foundation Impetus Grants, Startup funding from Columbia University: Taub Institute, Eli Lilly, MassCATS award, American Federation for Aging Research New Investigator Grant, Milton Fund.

Author Contributions

KVR and VP conceptualized the project and designed the methodology for all experiments. VP performed the majority of experiments. In addition, MS performed all stereotactic injections and in vivo surgeries, JB performed the proteomic screen in mice, NAS and CN designed and synthesized NMP-specific inhibitors, RM performed the majority of the IHC experiments and primary embryonic cultures, XW performed proteasome isolations, JF analyzed proteomic datasets, JN helped arrange figures, GM performed perfusion experiments for ApoE-TR experiments and blinded experimenters, MS prepared lipidated ApoE particles, HF maintained mouse crosses, DA, JN, XW, RM, CN, MS, and VP aided with writing and KVR did the majority of writing. BH provided ApoE human postmortem samples, DMH provided valuable reagents, and TN provided ApoE2, 3, and 4-KI mice as well as hTau/ApoE2, 3, and 4 double KI mice. KVR was responsible for acquiring funding and supervised the project.

Figures

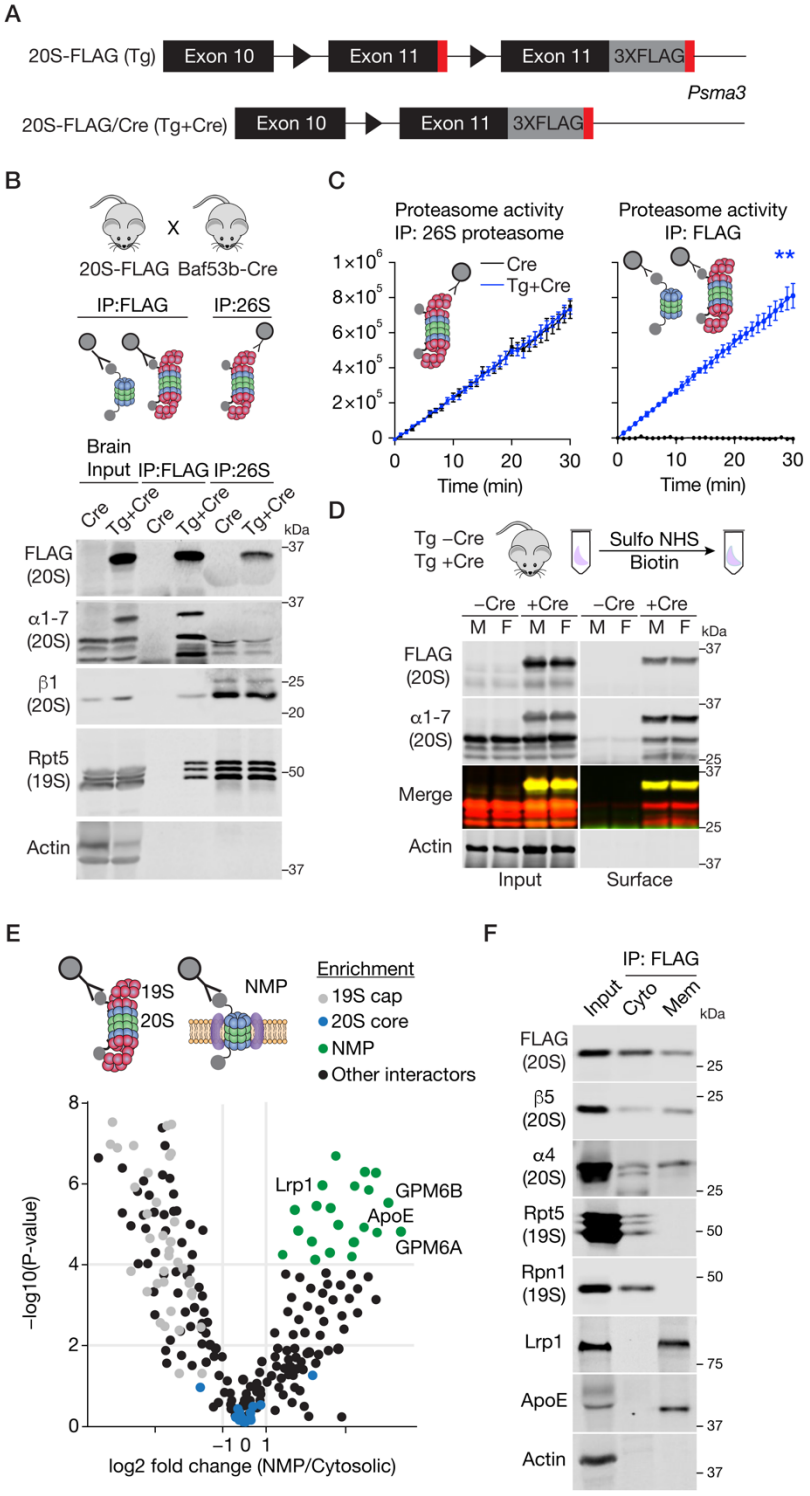

Figure 1
Paradise et al, 2022

Figure 1: NMPs co-purify with ApoE and Lrp1

a) Schematic for tagging the 20S proteasome with FLAG tag. Top (20S-FLAG, or Tg): the native Exon 11 of PSMA3 gene, containing the stop codon (red rectangle), was flanked with loxP sites (black triangles), and an insert containing 3x-FLAG tagged Exon 11 was added in the 3' UTR of the gene. Bottom (20S-FLAG/Cre, or Tg+Cre): in the presence of Cre, the native Exon 11 containing the stop codon was excised, enabling the expression of FLAG tag from the endogenous PSMA3 locus.

b) Immunoprecipitation (IP) of the proteasome from whole brains of Baf53b-Cre (Cre), or Baf53b-Cre/20S-FLAG Cre (Tg+Cre) mice using FLAG or 26S proteasomes affinity beads. Top: 20S-FLAG mice crossed with Baf53b-Cre mice to create the transgenic (Tg+Cre) line. Middle: diagram showing the proteasomal species targeted by different affinity beads; the FLAG beads target the FLAG-tagged 20S core particle, and the 26S beads target the 19S regulatory particle. Bottom: FLAG and 26S IP from mouse brain cytosolic fractions immunoblotted using indicated antibodies.

c) Comparison of proteolytic activity of proteasomes isolated by 26S IP and FLAG IP from whole brain cytosol shown in 1B by monitoring cleavage of model-substrate, Suc-LLVY-AMC. Proteasome-dependent cleavage of the substrate increases AMC fluorescence. Values represent averages from two technical replicates. *$p<0.01$ by Student's T-test.

d) Surface biotinylation and streptavidin pulldowns to isolate surface-exposed proteins. Top: diagram showing the surface biotinylation steps. Hippocampal tissues from mice (Tg-Cre or Tg+Cre) were dissected and subjected to surface biotin labeling using amine-reactive sulfo-NHS-biotin. Bottom: streptavidin pulldown of surface proteins in Tg- male (M) or female (F) mice, –/+ Cre. Lysates (input), and streptavidin pulldowns (surface) immunoblotted using antibodies against FLAG, α1-7 and cytosolic protein (actin). Merge indicates overlay (yellow) between FLAG (green) and α1-7 blots (red).

e) Co-IP and mass spectrometry (MS) analysis of 20S-FLAG proteasomes in cytosolic and membrane fractions from whole brains of Tg+Cre mice using anti-FLAG affinity beads. Differential levels of proteins enriched with membrane-associated NMP vs. cytosolic proteasomes were analyzed and plotted as log2-fold change vs –log10(P-value). Green dots represent proteins strongly enriched with the NMP Co-IP; blue dots represent 20S core subunits; gray dots represent proteins in 19S cap.

f) 20S-FLAG Co-IP from cytosolic (cyto) and membrane (mem) fractions of Tg+Cre mice immunoblotted using indicated antibodies.

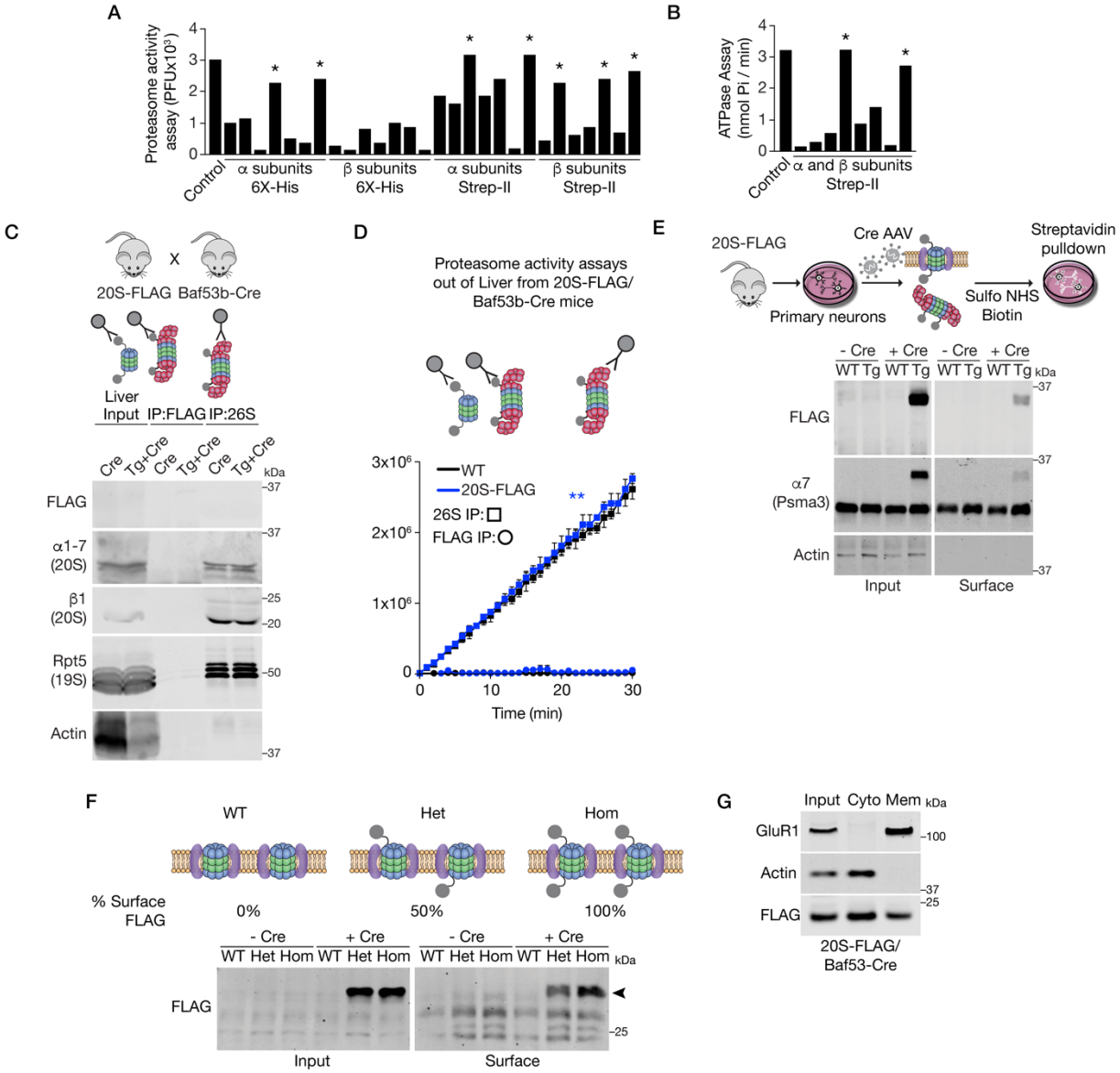

Supplemental Figure 1
Paradise et al., 2022

Supplemental Figure 1 NMPs co-purify with Apoe and Lrp1

a) Assessment of catalytic activity of epitope-tagged proteasomes in HEK293T cells. Cells were transfected with candidate constructs with epitope tags on the C-terminus of 11 20S subunits, and the 20S proteasomes were purified using Enzo Proteasome Purification Matrix. Proteasome catalytic activity was assessed by degradation of Suc-LLVY-AMC. Proteasome-dependent cleavage of the substrate increases AMC fluorescence.

b) Candidate hits from Fig S1A subjected to ATPase assay to measure the function of the 19S.

c) IP of the proteasome from liver tissues of Cre or Tg+Cre mice using FLAG or 26S proteasomes affinity beads. Top: 20S-FLAG mice crossed with Baf53b-Cre mice to create the transgenic (Tg+Cre) line. Middle: diagram showing the proteasomal species targeted by different affinity beads; the FLAG beads target the FLAG-tagged 20S core particle, and the 26S beads target the 19S regulatory particle. Bottom: FLAG and 26S IP from mouse liver cytosolic fractions immunoblotted using indicated antibodies.

d) Proteolytic activity of proteasomes isolated by 26S IP and FLAG IP shown in Fig S1C were compared by monitoring cleavage of model-substrate, Suc-LLVY-AMC. Values represent average from two technical replicates.

e) Validation of Cre-dependent expression of 20S-FLAG, using Synapsin-driven Cre expression by AAV transduction and surface biotinylation pulldown on streptavidin beads. Top: primary neurons from Tg mice were transduced with Cre AAV, and plasma membrane proteins were surface-biotinylated using sulfo-NHS-Biotin. The labeled proteins were pulled down using streptavidin. Bottom: Lysates (Input) and streptavidin pulldowns (Surface) were immunoblotted using the indicated antibodies.

f) Comparison of primary neurons, isolated from wild-type (WT), heterozygous (het) and homozygous (hom) 20S-FLAG transgenic mice. Transgene expression induced by Synapsin-drivin Cre. Top: diagram showing FLAG epitopes exposed to cell surface in accordance with FLAG genotype. Bottom: Lysates (input) and streptavidin pulldowns (Surface) were immunoblotted using anti-FLAG antibodies. Black arrow indicates FLAG expression.

g) Membrane fractionation of whole brains from Tg+Cre mice immunoblotted using indicated antibodies.

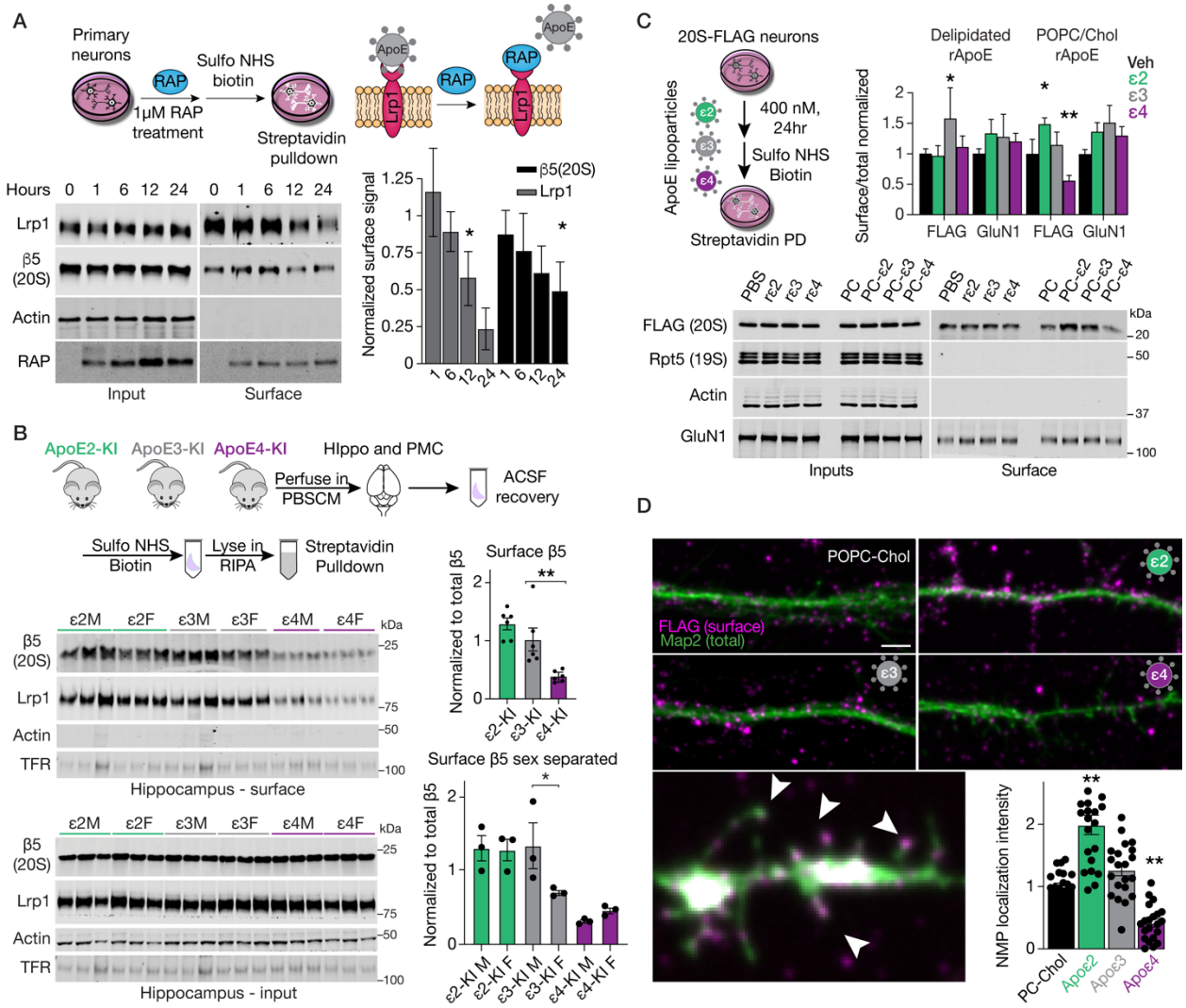

Figure 2
Paradise et al, 2022

Figure 2: ApoE isoforms differentially modulate NMP localization in vivo and in humans

(a) Schematic (left) shows surface biotinylation of Receptor-Associated Protein (RAP)-treated neurons. (Right) Influence of RAP on Lrp1-ApoE interaction is also depicted. DIV 13-14 primary cortical neurons were treated with 1 μM RAP for indicated times (hours). Treated neurons then subjected to surface biotinylation. Lysates (Input) and streptavidin pulldown (Surface) immunoblotted using indicated antibodies. Quantification of surface Lrp1 and B5 intensity graphed, N= 3 biological replicates, *p<0.01 by Two-Way ANOVA.

(b) Schematic of surface biotinylation experiments from ApoE isoform-knock in (KI) mice. Hippocampi (hippo) and Primary Motor Cortex (PMC) from ApoE2-KI (green), ApoE3-KI (gray), and ApoE4-KI (purple), male (M) and female (F) mice were subjected to surface biotinylation and streptavidin pulldown to isolate surface exposed proteins. Total lysates (Input) and Streptavidin pulldowns (Surface) from hippocampi were immunoblotted using indicated antibodies. Quantification of surface B5 intensity normalized to total B5 intensity graphed, N=6 biological replicates per genotype (3 males, 3 females), *p<0.01 by Two-Way ANOVA.

(c) Schematic of surface biotinylation experiment from postnatal primary cortical neurons from 20S-FLAG transgenic mice. DIV14 neurons were treated with 400 nM delipidated recombinant ApoE isoforms (rE2: green; rE3: gray; rE4: purple), or POPC/Cholesterol (POPC/Chol) lipoparticles conjugated with recombinant ApoE isoforms (PC-E2: green; PC-E3: gray; PC-E4: purple) for 24 hours and subjected to surface biotinylation. Total lysates (Input) and Streptavidin pulldowns (Surface) were immunoblotted using indicated antibodies. Quantification of surface FLAG and GluN1 intensities in neurons treated with delipidated and POPC/Chol recombinant ApoE particles graphed. Intensities of surface FLAG and GluN1 were normalized to total FLAG and GluN1 intensities. N=3 biological replicates, *p<0.05, **p<0.01 by Two-Way ANOVA.

(d) Representative images from antibody feeding experiments. DIV14 neurons from 20S-FLAG transgenic mice. Neurons were treated with lipidated ApoE2 (green), ApoE3 (gray), and ApoE4 (purple). FLAG antibodies were fed on live neurons to mark surface localizations (FLAG Surface); subsequently neurons were fixed and stained for Map2 (Total). Antibodies used were FLAG (NMP signal) and Map2 (total proteins). Quantification of NMP localization intensity graphed, N=3 biological replicates, n=19 quantified regions, *p<0.01 by Two-Way ANOVA.

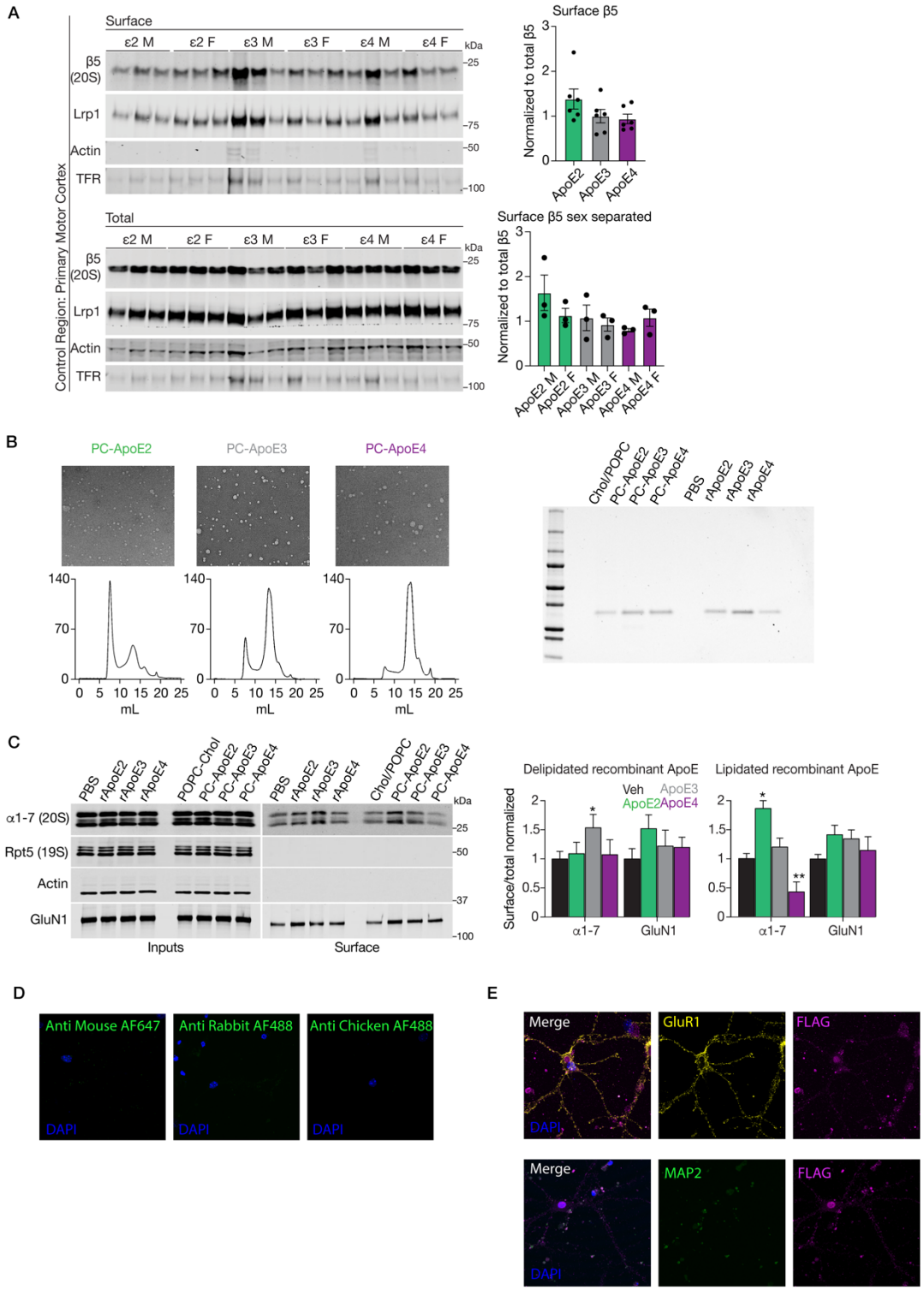

Supplemental Figure 2
Paradise et al., 2022

Supplemental Figure 2: ApoE isoforms differentially modulate NMP localization in vivo and in humans

(a) Surface biotinylation experiments from ApoE isoform-knock in (KI) mice. Hippocampi (hippo) and Primary Motor Cortex (PMC) from ApoE2-KI (green), ApoE3-KI (gray), and ApoE4-KI (purple), male (M) and female (F) mice were subjected to surface biotinylation and streptavidin pulldown to isolate surface exposed proteins. Total lysates (Input) and Streptavidin pulldowns (Surface) from PMC were immunoblotted using indicated antibodies. Quantification of surface B5 intensity normalized to total B5 intensity graphed, N=6 biological replicates per genotype (3 males, 3 females), *$p<0.01$ by Two-Way ANOVA.

(b) Representative images from negative staining EM (top) of ApoE lipoparticles ApoE2 (green), ApoE3 (gray) and ApoE4 (purple) and their corresponding chromatograms from size-exclusion chromatography (bottom). (Right) Coomassie G250 stained gel comparing PC-ApoE isoforms and non-lipidated recombinant ApoE isoforms.

(c) DIV14 neurons from WT mice were treated with 400 nM delipidated recombinant ApoE isoforms (rE2: green; rE3: gray; rE4: purple), or POPC/Cholesterol (POPC/Chol) lipoparticles conjugated with recombinant ApoE isoforms (PC-E2: green; PC-E3: gray; PC-E4: purple) for 24 hours and subjected to surface biotinylation. Total lysates (Input) and Streptavidin pulldowns (Surface) were immunoblotted using indicated antibodies. Quantification of surface 20S and GluN1 intensities in neurons treated with delipidated and POPC/Chol recombinant ApoE particles graphed. Intensities of surface 20S and GluN1 were normalized to total 20S and GluN1 intensities. N=3 biological replicates, *$p<0.05$, **$p<0.01$ by Two-Way ANOVA.

(d) Representative images from antibody feeding experiments. DIV14 neurons from 20S-FLAG transgenic mice. Only secondary antibodies were used.

(e) Representative images of antibody feeding experiments using DIV14 neurons from 20S-FLAG transgenic mice. FLAG, GluR1 (Surface) and MAP2 (Intracellular) antibodies were fed on live neurons for antibody feeding permeability control.

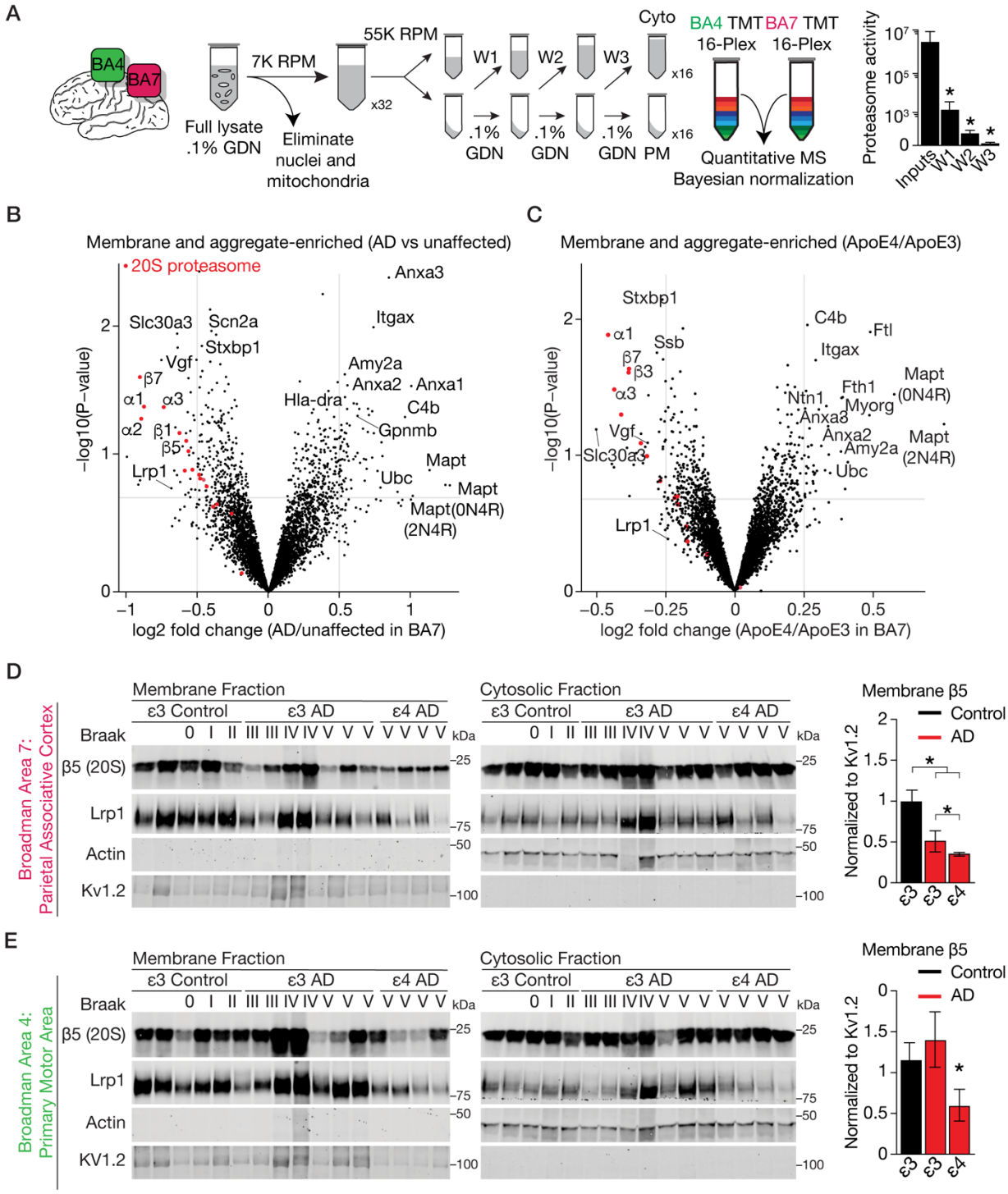

Figure 3
Paradise et al 2022

Figure 3. NMP localization is reduced in vulnerable brain regions in the human brain and is further reduced by ApoE4 genotype

a) Schematic depicting steps to enrich plasma membrane and protein aggregates from post-mortem human brain tissues. Brodmann Area 7 (BA7, red) and BA4 (green) regions of the human brain fractionated to obtain crude membrane and aggregate fractions, which were then washed 3 times (W1, W2, W3). Supernatants from washes pooled to generate cytosolic fractions (Cyto) and membrane and aggregate enriched fractions (PM). Samples labeled with Tandem Mass Tags (TMT) for quantitative MS analysis. Cytosolic contamination assessed by the proteasome activities of the washes graphed (right). N=32, *$p<0.001$ by Paired T-Test.

b) Determining effect of AD on the plasma membrane and detergent-insoluble proteome. Differential enrichment of plasma membrane and detergent-insoluble proteins in AD vs. unaffected patients in the BA7 region was analyzed and plotted as log2-fold change vs –log10(P-value). Samples were prepared as described in 3A. Red dots indicate 20S proteasome subunits.

c) Determining effect of ApoE genotype on the plasma membrane and detergent-insoluble proteome. Differential enrichment of plasma membrane and detergent-insoluble proteins in ApoE4 vs ApoE3 patients in the BA7 regions was analyzed and plotted as log2-fold change vs –log10(P-value). Samples were prepared as described in 3A. Red dots indicate 20S proteasome subunits.

d) Determining effect of AD and ApoE genotype on NMP localization from the BA7 (red) region. Membrane and cytosolic fractions from BA7 regions immunoblotted using indicated antibodies. Braak stages indicated above. Samples were prepared as described in 3A. Levels of z20S subunit β5 and Lrp1 in the membrane fractions were assessed in AD patients, and in ApoE3 and ApoE4 genotypes. The band intensities for β5 were quantified and normalized to the loading control Kv1.2, and the averages were plotted in the bar graph to the right; error bars represent S.D.

e) Determining effect of AD and ApoE genotype on NMP localization from the BA4 (green) region. Membrane and cytosolic fractions from BA4 regions immunoblotted using indicated antibodies. Braak stages indicated above. Samples were prepared as described in 3A. Levels of 20S subunit β5 and Lrp1 in the membrane fractions were assessed in AD patients, and in ApoE3 and ApoE4 genotypes. The band intensities for β5 were quantified and normalized to the loading control Kv1.2, and the averages were plotted in the bar graph to the right; error bars represent S.D.

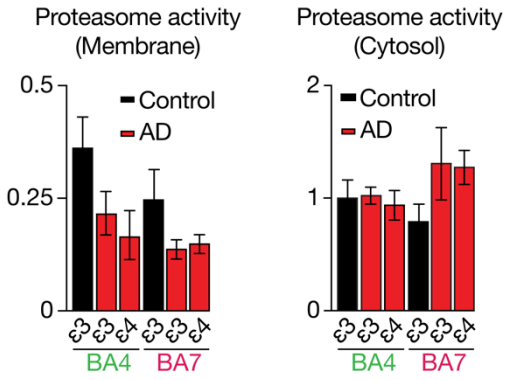

Figure S3
Paradise et al 2022

Figure S3. Supplementary to Figure 3: NMP localization is reduced in vulnerable brain regions in the human brain and is further reduced by ApoE4 genotype.

Proteasome catalytic activities of membrane and cytosolic fractions from brain tissues of AD patients of ApoE3 and ApoE4 genotypes in BA4 and BA7. Proteasome activities were assessed by degradation of the substrate Suc-LLVY-AMC. Proteasome-dependent cleavage of the substrate increases AMC fluorescence.

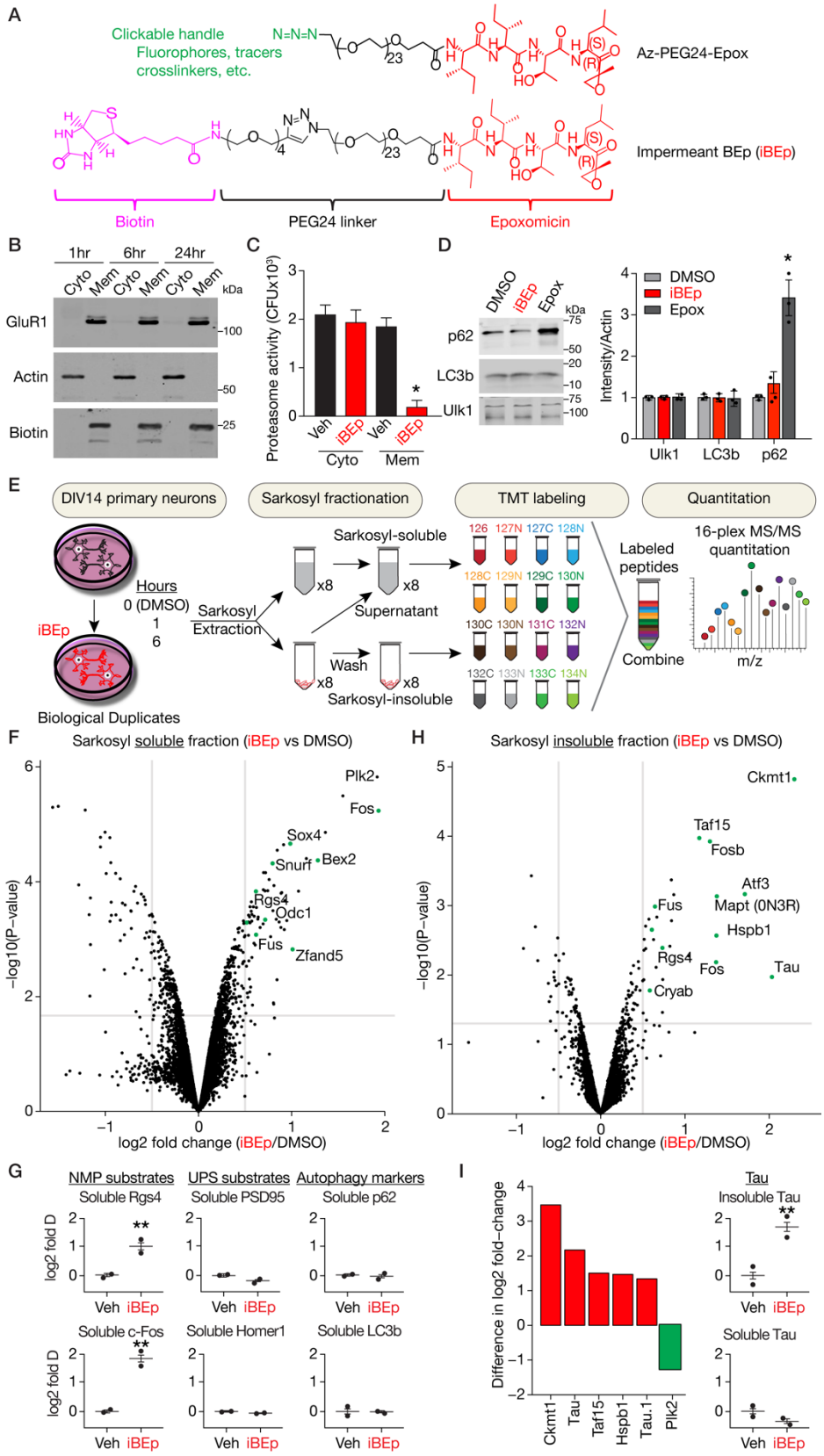

Figure 4, Paradise et al 2022

Figure 4: Selective NMP inhibition induces endogenous Tau aggregation
(a) Top: Structure of the 'Clickable' epoxomicin handle. Bottom: Structure of the NMP-specific proteasome inhibitor impermeant biotin epoxomicin (iBEp).

(b) Primary cortical neurons were treated with 1 μM iBEp for 1, 6 and 24 hours and subjected to membrane fractionation. Cytosolic (Cyto) and membrane (Mem) fractions were immunoblotted using indicated antibodies.

(c) Proteasome catalytic activities of membrane and cytosolic fractions from neurons treated with iBEp. Proteasome catalytic activity was assessed by degradation of Suc-LLVY-AMC; proteasome-dependent cleavage of the substrate increases AMC fluorescence. DIV 14 Primary Cortical neurons treated with DMSO Vehicle (Veh, Black) and 1μM iBEp (red) for 6 hours. N=3 biological duplicates, *$p<0.001$ by Two-Way ANOVA.

(d) Lysate from DIV 14 primary cortical neurons treated with DMSO (light gray), iBEp (red) or Epoxomicin (Epox, dark gray) immunoblotted using antibodies against common autophagy markers: p62, LC3b, and Ulk1. Quantification of the markers intensity normalized to actin intensity graphed. N=4 biological replicates, *$p<0.01$ by Two-Way ANOVA.

(e) Schematic depicting fractionation to analyze changes in sarkosyl soluble and insoluble proteomes in response to NMP inhibition. DIV14 primary neurons were treated with DMSO or 1μM iBEp for 1 and 6 hours, then subjected to sarkosyl fractionation. Sarkosyl-soluble and insoluble fractions were labeled with Tandem Mass Tags (TMT) to enable quantitative proteomic analysis.

(f) Differential enrichment of proteins in the sarkosyl-soluble fraction of neurons treated with iBEp versus with DMSO were analyzed and plotted as log2-fold change vs –log10(P-value). Green dots represent proteins enriched in the iBEp treatment compared to DMSO treatment.

(g) Graphs plotting the log2 fold change of select proteins which are NMP substrates, UPS substrates and autophagy markers enriched in the soluble fraction from neurons treated with iBEp vs. DMSO (Veh). ***$p<0.05$ (adjusted p-value after multiple corrections).

(h) Differential enrichment of proteins in the sarkosyl-insoluble fractions of neurons treated with iBEp versus DMSO were analyzed and plotted as log2-fold change vs –log10(P-value). Green dots represent proteins enriched in the iBEp treatment compared to DMSO treatment.

(i) (Left) Identification of proteins which are exclusively enriched in the insoluble fraction with no corresponding change in the soluble fraction (red). Plk2 represents the only protein which is enriched in the soluble fraction with no corresponding change in the insoluble fraction (green). most significant changes in levels in sarkosyl-insoluble fractions relative to sarkosyl

soluble fractions from neurons treated with iBEp, plotted as differences in log2 fold changes. (Right) Log2 fold changes of insoluble Tau (top) and soluble Tau (bottom) enriched in neurons treated with DMSO (Veh) vs. iBEp graphed. ***$p<0.05$ (adjusted p-value after multiple corrections).

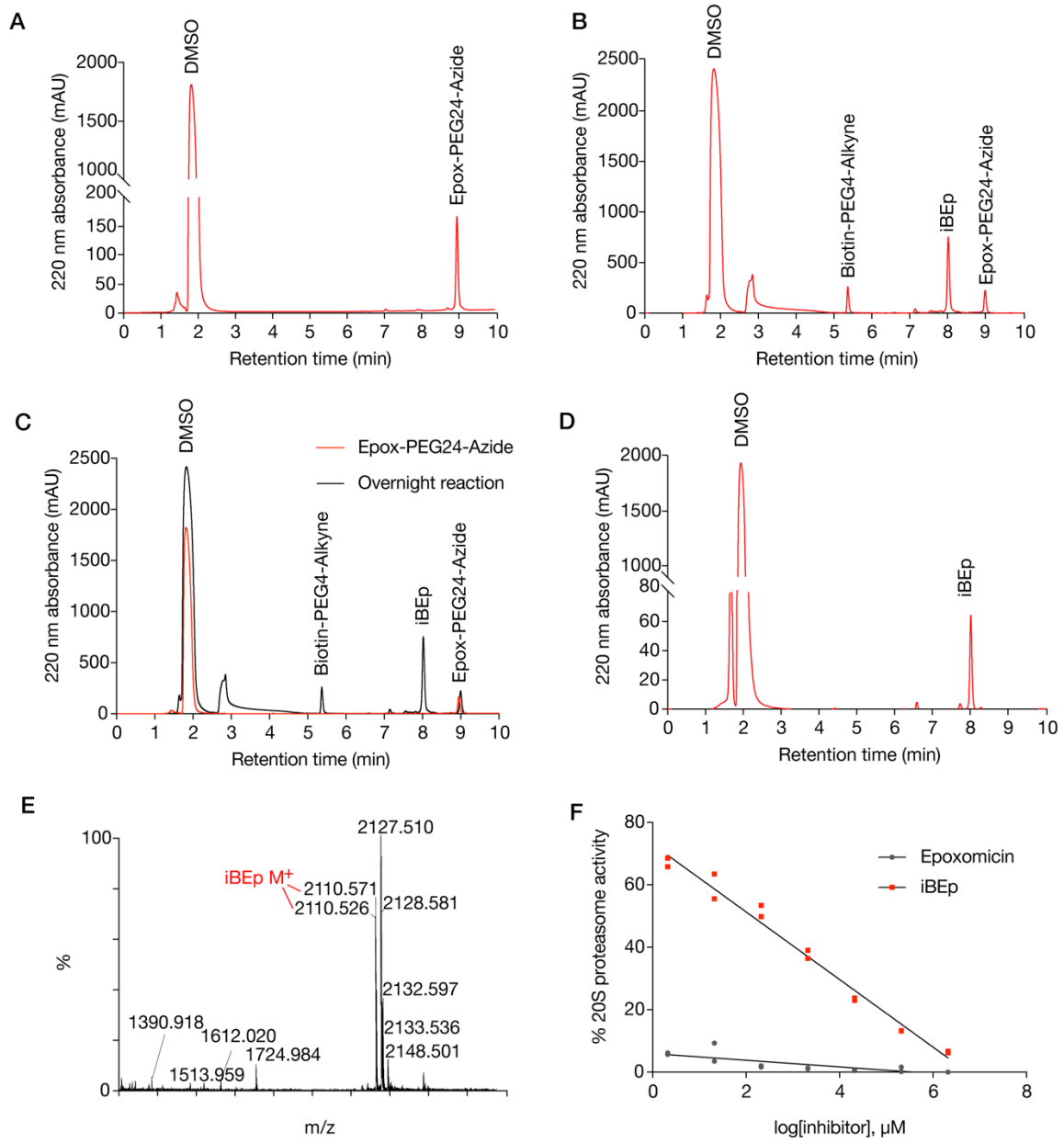

Figure S4
Paradise et al 2022

Figure S4. Supplementary to Figure 4. Quantitative proteomics reveals that selective inhibition of NMPs induces Tau aggregation.

(a) HPLC analysis for Epox-PEG24-azide.

(b) HPLC analysis for the overnight reaction between biotin-PEG4-alkyne and Epox-PEG24-azide.

(c) Overlay of S4A and S4B. Note the emergence of peak at 8 minutes corresponding to the formation of iBEp after overnight reaction.

(d) HPLC analysis of iBEp after purification.

(e) LC/MS spectrum of purified iBEp. Expected mass of iBEp (2110.54) is observed. Other peaks correspond to adducts resulting from LC/MS ionization in the spectrometer.

(f) Proteasome catalytic activity assay using HEK293T-LentiX lysate comparing inhibitory effects of a dose curve of iBEp (red) and epoxomicin (dark gray). Catalytic activity was assessed by degradation of Suc-LLVY-AMC; proteasome-dependent cleavage of the substrate increases AMC fluorescence.

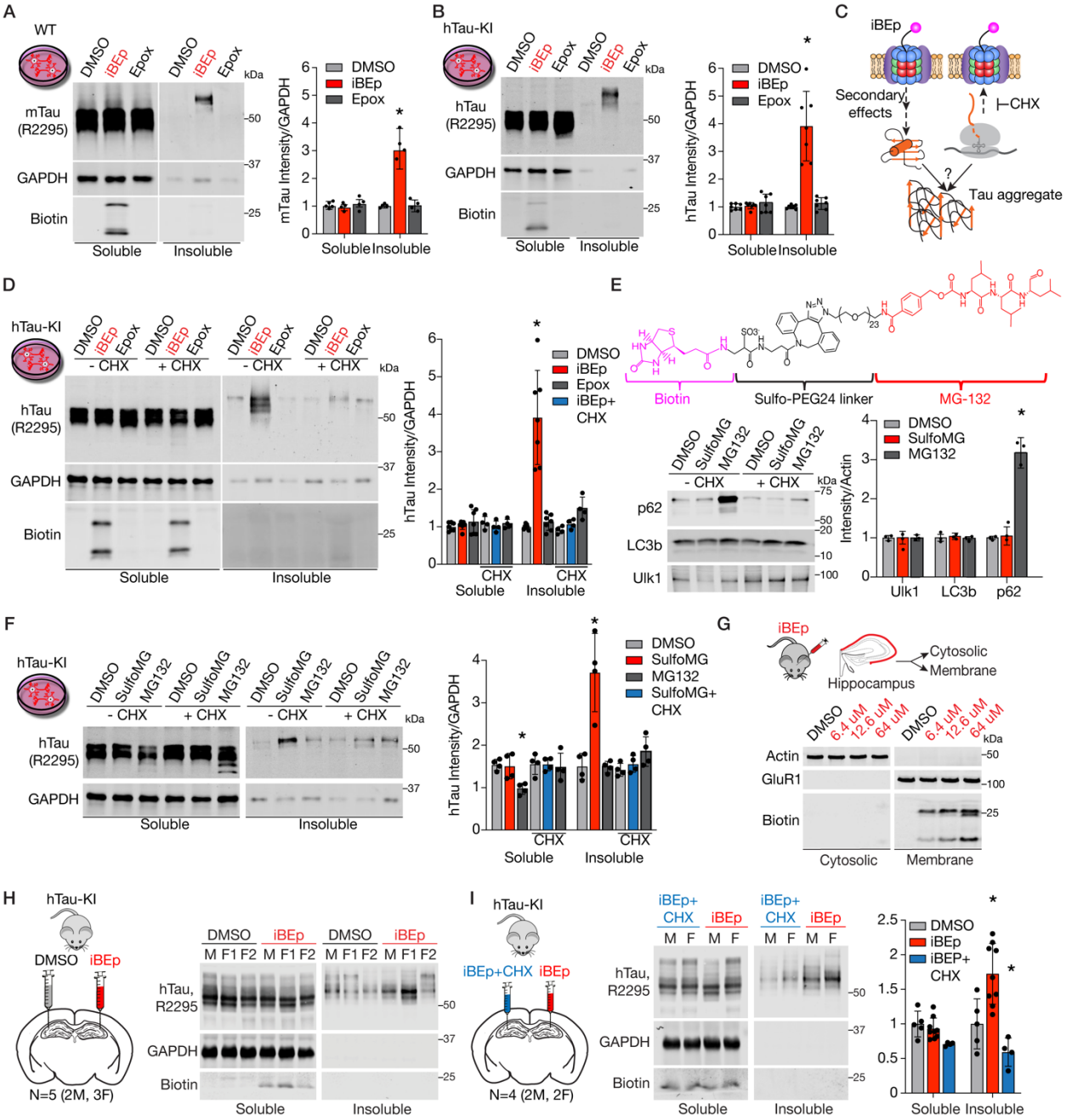

Figure 5
Paradise et al 2022

Figure 5: NMPs are licensed to degrade newly synthesized endogenous Tau in vitro and in vivo

a) Sarkosyl-soluble (Soluble) and sarkosyl-insoluble (Insoluble) fractions in DIV 14 primary cortical neurons from wild-type (WT) mice, treated with 1μM iBEp (red) or 10 μM Epoxomicin (Epox, dark gray), immunoblotted using indicated antibodies and fluorescent streptavidin (biotin signal). Note doublet represents covalent modification of proteasome catalytic subunits with iBEp. Quantifications for band intensities, normalized using GAPDH loading control, are plotted in the bar graph to the right, N=5 biological replicates, error bars representing S.D., *p<0.001 by Two-Way ANOVA.

b) Sarkosyl-soluble (Soluble) and sarkosyl-insoluble (Insoluble) fractions in DIV 14 primary cortical neurons from human Tau Knock In (hTau-KI) mice, as treated in Figure 5A, immunoblotted using indicated antibodies and fluorescent streptavidin (biotin signal). Note doublet represents covalent modification of proteasome catalytic subunits with iBEp. Quantifications for band intensities, normalized using GAPDH loading control, are plotted in the bar graph to the right, N=7 biological replicates, error bars representing S.D., *p<0.001 by Two-Way ANOVA.

c) Schematic depicting two models by which NMP inhibition can induce aggregation of Tau.

d) Sarkosyl-soluble (Soluble) and sarkosyl-insoluble (Insoluble) fractions in DIV 14 primary cortical neurons from hTau-KI mice, treated with iBEp (red) or epoxomicin (Epox, dark gray) as in Figure 5A, with or without cycloheximide (CHX,10 μg/mL), immunoblotted using indicated antibodies and fluorescent streptavidin (biotin signal). Note doublet represents covalent modification of proteasome catalytic subunits with iBEp. Quantifications for band intensities, normalized using GAPDH loading control, are plotted in the bar graph to the right, N=7 biological replicates, error bars representing S.D., *p<0.001 by Two-Way ANOVA.

e) (Top) Structure of Sulfo-MG132 (Sulfo-MG). (Bottom) DIV 14 primary neurons treated with Sulfo-MG132 (1 μM), or MG132 (10 μM), with or without cycloheximide (CHX, 10 μg/mL), immunoblotted using antibodies against autophagy markers p62, LC3B and Ulk1. Quantifications for band intensities, normalized using actin loading control, are plotted in the bar graph to the right for N=3 biological replicates, error bars representing S.D., *p<0.001 by Two-Way ANOVA.

f) Sarkosyl-soluble (Soluble) and sarkosyl-insoluble (Insoluble) fractions in DIV 14 primary cortical neurons from hTau-KI mice, treated as in Figure 5E with Sulfo-MG132 or MG132, with or without cycloheximide (CHX), immunoblotted using indicated antibodies. Quantifications for band intensities, normalized using GAPDH loading control, are plotted in the bar graph to the right for N=4 biological replicates, error bars representing S.D., *p<0.01 by Two-Way ANOVA.

(g) Analysis of the effects of iBEp on NMP level *in vivo*. (Top) iBEp (6.4, 12.6 and 64 μM) was stereotactically injected into the hippocampus in the left hemisphere of wild type mice and hippocampi were subject to membrane fractionation. (Bottom) Cytosolic and membrane fractions immunoblotted using indicated antibodies and fluorescent streptavidin (biotin signal). Note that the biotin signal only appears in the membrane fraction.

h) hTau-KI mice were injected with iBEp (12.6 μM) in the hippocampus of the left hemisphere and DMSO contralaterally, and the hippocampi were subjected to sarkosyl extraction. The sarkosyl-soluble (Soluble) and sarkosyl-insoluble (Insoluble) fractions were immunoblotted using indicated antibodies and fluorescent streptavidin. Quantifications for band intensities, normalized using GAPDH loading control, are plotted in the bar graph to the right in Figure 5I, N= 5 biological replicates; (2M, 3F), *$p<0.001$ by Two-Way ANOVA.

i) hTau-KI mice were injected with iBEp (12.6 μM) in the hippocampus of the left hemisphere and (iBEp+CHX) (12.6 μM/ 1.77 μM) contralaterally, and the hippocampi were subjected to sarkosyl extraction. The sarkosyl-soluble (Soluble) and sarkosyl-insoluble (Insoluble) fractions were immunoblotted using indicated antibodies and fluorescent streptavidin. Quantifications for band intensities, normalized using GAPDH loading control, are plotted in the bar graph to the right for N=4 biological replicates (2M, 2F), error bars representing S.D., *$p<0.001$ by Two-Way ANOVA.

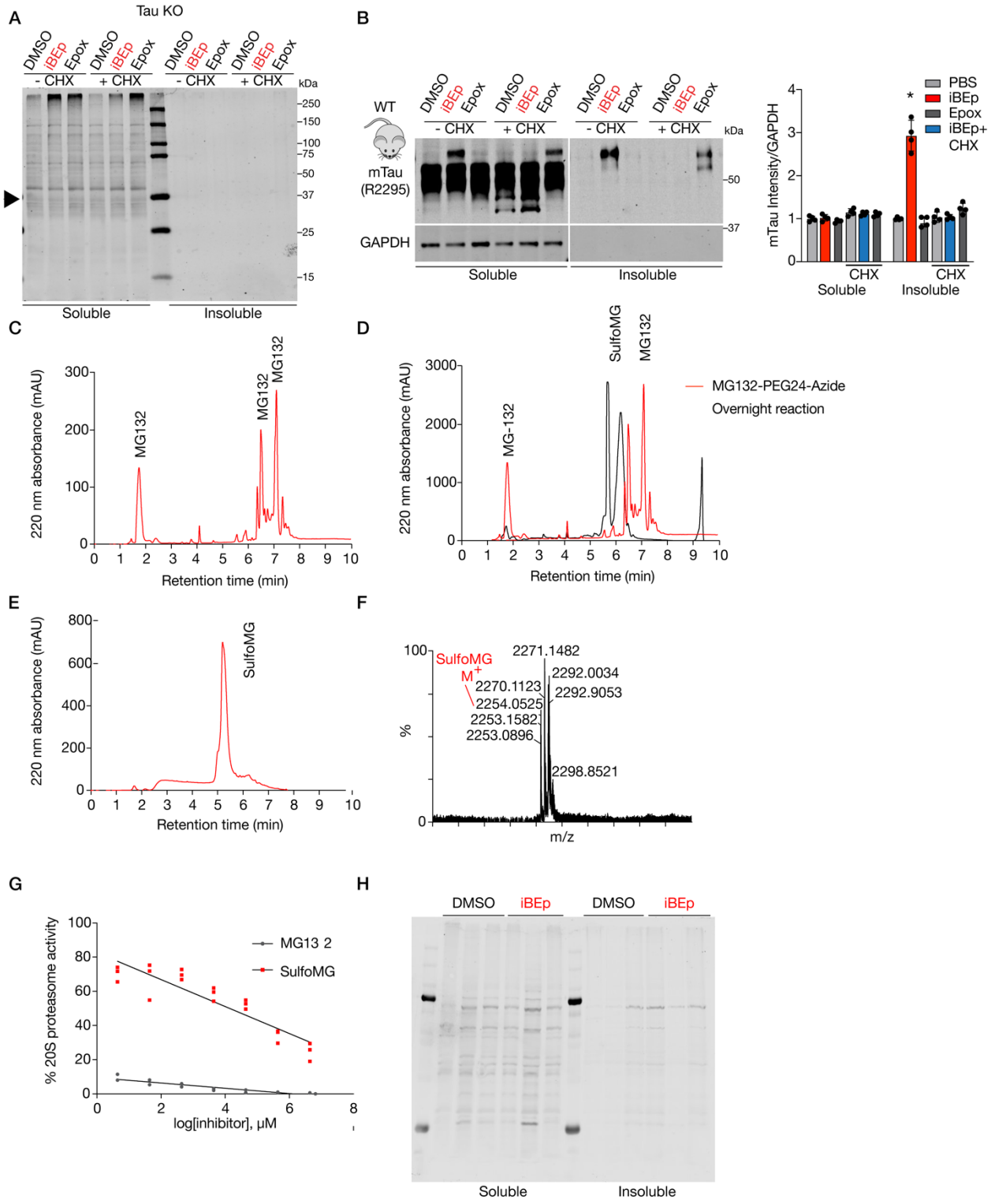

Figure S5
Paradise et al, 2022

Figure S5. Supplementary to Figure 5: NMPs are licensed to degrade newly synthesized endogenous Tau in vitro and in vivo.

a) Validation of anti-Tau antibody (R2295) specificity in primary neurons from Tau KO mice. Cells were treated as in Figure 5A with iBEp or Epoxomicin (Epox), with or without cycloheximide (CHX), and were subjected to sarkosyl extraction. Sarkosyl-soluble (Soluble) and Sarkosyl-insoluble (Insoluble) fractions were immunoblotted using anti-Tau antibody R2295. We do not observe any signal at the expected molecular weight for Tau as indicated by the black arrow.

b) Validation of anti-Tau antibody (R2295) specificity in primary neurons from wild-type (WT) mice. Cells were treated as in Figure 5A with iBEp (red) or Epoxomicin (Epox, dark gray),with or without cycloheximide (CHX), and were subjected to sarkosyl extraction. Sarkosyl-soluble (Soluble) and Sarkosyl-insoluble (Insoluble) fractions were immunoblotted using anti-Tau antibody R2295. Quantifications for band intensities, normalized using GAPDH loading control, are plotted in the bar graph to the right for N=4 biological replicates, error bars representing S.D. *$p<0.001$ by Two-Way ANOVA.

c) HPLC analysis of MG132-PEG24-Azide.

d) Overlay of HPLC chromatograms of MG132-PEG24-Azide (red) and the overnight reaction between MG132-PEG24-Azide and DBCO-Sulfo-Link-Biotin (black). Note peaks emerging at 5.5 and 6 minutes corresponding to the formation of Sulfo-MG132 (Sulfo-MG).

e) HPLC analysis of Sulfo-MG132 after purification.

f) LC/MS spectrum of purified Sulfo-MG132. Expected mass of Sulfo-MG132 (2254.0525) is observed. Other peaks correspond to adducts resulting from LC/MS ionization in the spectrometer.

g) Proteasome catalytic activity assay using HEK293T-LentiX lysate comparing inhibitory effects of a dose curve of MG132 (green) and Sulfo-MG132 (orange). Catalytic activity was assessed by degradation of Suc-LLVY-AMC; proteasome-dependent cleavage of the substrate increases AMC fluorescence.

h) Tau-KO Mice (N=3, 2M, 1F) were injected with iBEp (12.6 μM) in the hippocampus of the left hemisphere and DMSO contralaterally. The hippocampi were subjected to sarkosyl extraction. The sarkosyl-soluble (Soluble) and sarkosyl-insoluble (Insoluble) fractions in Tau-KO mice were immunoblotted using anti-Tau antibody R2295. We do not observe any signal at the expected molecular weight for Tau as indicated by the black arrow.

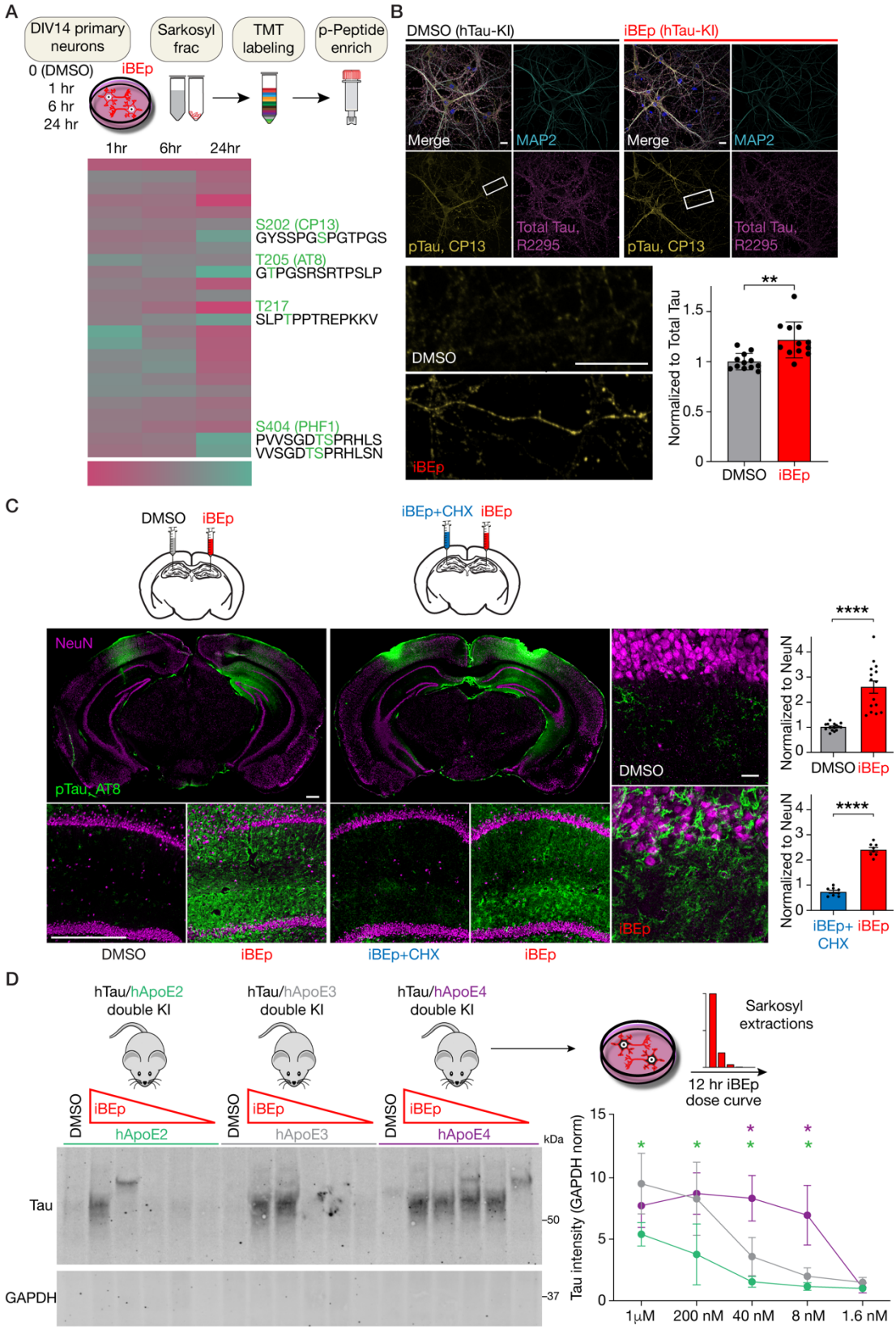

Figure 6
Paradise et al 2022

Figure 6: NMP complexes determine the ApoE-isoform dependent risk for Tau aggregation and pathology in vivo

(a) (Top) Schematic of quantitative phosphoproteomics experiments from primary neurons treated with NMP-specific inhibitor iBEp. DIV14 primary neurons treated with 1μM iBEp or DMSO separated into sarkosyl soluble (gray) or insoluble (red) fractions. Peptides were labeled with TMT to enable quantitative phosphoproteomic analysis. (Bottom) Heatmap displays all identified Tau phosphopeptides and their relative depletion (red) or enrichment (green) of phosphopeptides compared to DMSO controls over indicated timecourse.

(b) Immunocytochemical analysis of DIV14 primary hippocampal neurons from human Tau-knockin (hTau-KI) mice treated with 1μM iBEp or DMSO for 12 hours. Neurons stained using indicated antibodies: MAP2 (blue) to label dendrites, phosphorylated Tau (pTau, CP13, yellow) or total Tau (R2295, purple). Quantification of pTau signal intensity normalized to total Tau. N=12 coverslips from three separate biological replicates and dissections. Mean ± SEM, **$p < 0.01$ by Paired T-test. Scale Bars = 15 μm

(c) Four-to-five month old hTau-KI mice were stereotactically injected with iBEp (red, 6.4μM) into the CA1 region of the hippocampus in the left hemisphere and PBS (gray) contralaterally injected. In separate mice, iBEp alone (6.4μM, red) was injected into the CA1 region in the hippocampus of the left hemisphere and iBEp +CHX (6.4μM/1.7mM, blue) contralaterally injected. Mice collected 72 hours post injection. Sections were stained using indicated antibodies: NeuN (purple) and AT8 (pTau signal, green). 4X, 20X and 60X representative images are shown. Quantification of pTau signal intensity graphed, N=5 mice (3F, 2M), n=3 slices/animal, N=4 (3F,1M), n=2 slice/animal. ****$p<0.0001$ by Paired T-test/experiment,

(d) DIV14 primary neurons from hTau/hApoE2 double knockin (green), hTau/hApoE3 double knockin (gray), and hTau/hApoE4 double knockin (purple) mice were incubated with a range of iBEp (red) doses from 1000 to 1.6nM, and were subject to sarkosyl extraction. Sarkosyl-insoluble fractions were immunoblotted using indicated antibodies. Quantification of sarkosyl-insoluble Tau intensity graphed, N=3 biological replicates, *$p<0.01$ by Two-Way ANOVA Tukey's multiple comparisons test.

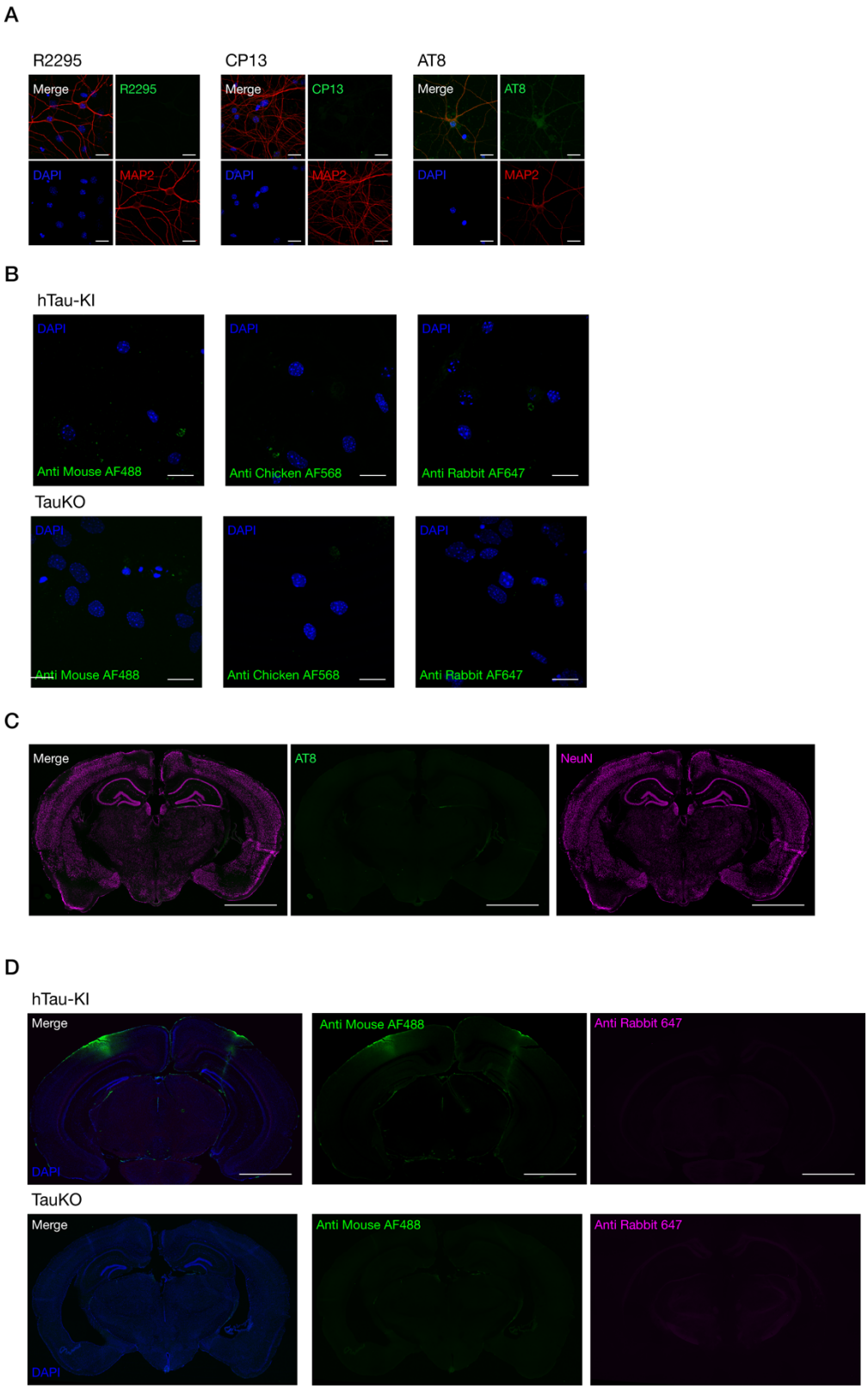

Figure S6
Paradise et al 2022

Supplemental Figure 6: NMP complexes determine the ApoE-isoform dependent risk for Tau aggregation and pathology in vivo

a) Immunocytochemical analysis of DIV 14 primary hippocampal neurons from Tau-KO mice. Neurons stained using indicated antibodies and DAPI. Scale bars indicate 20 µm.

b) Immunocytochemical analysis controls of DIV 14 primary hippocampal neurons from hTau-KI (top) and TauKO (bottom) mice, using only secondary antibodies. Scale bars indicate 20 µm.

c) Immunohistochemical analysis of Tau-KO mice using anti-pTau antibodies AT8 (green) and NeuN (purple). Scale bars indicate 1 mm.

d) (Top) Immunohistochemical analysis of hTau-KI mice, injected with iBEp (12.6 µM) in the hippocampus of the left hemisphere and DMSO contralaterally, using only secondary antibodies. (Bottom) Immunohistochemical analysis of Tau-KO mice, using only secondary antibodies. Scale bars indicate 1 mm.

Methods

Antibodies

Antibody	Vendor	Catalog	Application	Dilution
M anti actin	Abcam	ab8226	WB	1:1000
R anti actin	Abcam	ab8227	WB	1:1000
R anti PSMB5	Bethyl	A303-847A	WB	1:1000
R anti PSMA3	Proteintech	11887-1-AP	WB	1:1000
M anti alpha 1-7	Enzo	MCP231	WB	1:1000
R anti GluR1	Cell Signaling	13185S	WB Ab feeding	1:1000 1:100
M anti TFR	Abcam	ab1086	WB	1:1000
R anti TFR	Abcam	ab84036	WB	1:1000
M anti GAPDH	Santa Cruz	sc-32233	WB	1:2500
M anti flag M2	Sigma	F1804	WB Ab feeding	1:1000 1:100
M anti his tag	Genetech	A00186	WB	1:1000
M anti strepII tag	Genetech	A01732	WB	1:1000
R anti Rpt5	Bethyl	A303-538A	WB	1:1000
R anti Rpn13	Abcam	Ab157218	WB	1:1000
Ch anti MAP2	Thermo	PA-10005	ICC	1:1000
R anti Tau (R2295)	V. Lee	N/A	WB ICC	1:1000 1:1000
M anti pTau (CP13)	Albert Einstein/P. Davies	N/A	ICC	1:2500
M anti pTau (AT8)	ThermoFisher	MN1020	ICC IHC	1:2500 1:1000
R anti NeuN	Sigma	ABN78	IHC	1:1000
M anti KV2.1	DSHB	K14/16	WB	1:1000
R anti PSMB1	ProteinTech	11749-1-AP	WB	1:1000
R anti Lrp1	Abcam	ab92544	WB	1:1000
p62	Abcam	ab109012	WB	1:1000
LC3b	Abcam	ab48394	WB	1:1000
Ulk1	Sigma	A7481	WB	1:1000
Anti mouse IgG 680 LT	Licor	926-68022	WB	1:10,000
Anti Rat IgG 680 RD	Licor	925-68076	WB	1:10,000
Anti Rabbit IgG 800 CW	Licor	926-32211	WB	1:10,000
Streptavidin 680 LT	Licor	926-68031	WB	1:10,000
Anti rabbit IgG AF647	ThermoFisher	A21244	ICC	1:1000

Anti mouse IgG AF488	ThermoFisher	A11001	ICC	1:1000
Anti mouse IgG AF647	ThermoFisher	A21240	ICC	1:1000
Anti chicken IgY AF488	ThermoFisher	A32931	ICC	1:1000
Anti chicken IgY AF568	ThermoFisher	A78950	ICC	1:1000

Generation of tagged 20S DNA constructs

Plasmids containing full length mouse PSMA1, 2, 3, 7, and PSMB1, 2, 3, 4, 5, 6, and 7 were acquired from Dharmacon Inc. 6XHis and StrepII constructs were designed as c-term tags with GGS and GGA linkers, respectively and were cloned into pCAGEN (Addgene 11160) for transfection and pLenti hSynapsin Cre WPRE (Addgene 86641) for lentivirus production. Q5 DNA polymerase (NEB) was used in PCRs to amplify proteasome subunit sequences with respective tags using PCR conditions recommended by the manufacturer. Amplified fragments were run on a 1% agarose gel and visualized to confirm PCR and purified with a commercial kit (Machery Nagel). pCAGEN was digested with EcoRV (NEB) and pLenti hSynapsin Cre WPRE was digested with AgeI and EcoRI (NEB). Digested plasmids were run on a 1% agarose gel and gel extracted using a standard kit (Machery Nagel). Purified vectors and fragments were assembled using Gibson assembly (NEB) and constructs were transformed into competent cells, NEB5α competent cells (NEB) for pCAGEN constructs, and NEBStable competent cells (NEB) for pLenti. Single colonies were sequence verified using Sanger sequencing and preserved in glycerol stocks. All plasmids used in this study were grown up and purified using standard kits from commercial vendors.

Lentiviral production

LentiX293T cells were transfected using the standard protocol in normal culture medium with polyethylenimine (PEI). Cells were transfected with PEI, envelope pMD2.G (Addgene 12259), packaging psPAX2 (Addgene 12260) and transfer plasmid. As per the standard protocol, the media was aspirated and replaced with OptiMEM (Gibco) supplemented with 10 mM sodium butyrate (Sigma) and 1 mM sodium pyruvate (Sigma) 24 hours post transfection and collected 72 after transfection. The virus-containing media was concentrated with LentiX Concentrator (Takara) and resuspended in Neurobasal (Gibco).

Transfection and Transduction

HEK293T and LentiX293T cells were transfected using a polyethylenimine (PEI) protocol. Primary neurons were transfected using lipofectamine 2000 (Invitrogen) according to the manufacturer's protocol. iSyn Cre AAV was obtained from the Columbia University Zuckerman Institute Virology Core.

Cell Culture

HEK293T-LentiX cells (Takara 632180) were cultured in DMEM supplemented with 10% fetal bovine serum (Corning), 2 mM glutamine, 1 mM sodium pyruvate (Sigma) and

penicillin/streptomycin (100 U/mL and 100 µg/mL respectively). For wildtype primary cultures, E17 C57Bl/6 mouse cortical and hippocampal neurons were maintained in Neurobasal Medium (Gibco) supplemented with 2% B-27 (Gibco), penicillin/streptomycin (100 U/mL and 100 µg/mL respectively), and 2 mM glutamine. For transgenic primary cultures, P0-1 postnatal mouse cortical or hippocampal neurons were maintained in Neurobasal-A Medium (Gibco) supplemented with 2% B-27, penicillin/streptomycin (100 U/mL and 100 µg/mL respectively), and 2 mM glutamine. Standard neuronal culture protocols were followed to harvest and grow the cell and neuronal cultures.

Subsequent generations were confirmed by genotyping.

Mice

All animal procedures were performed under protocols compliant and approved by the Institutional Animal Care and Use Committees of Columbia University Medical Center. Wildtype mice (C57BL/6J, stock number 027 from Charles River Laboratories) and mice transgenic for 20S-flag$^{flox/flox}$, BAF53b Cre[29] (RRID: IMSR_JAX:027826), Tau knockout[87] (RRID: IMSR_JAX:007251), hTau KI[66], ApoE2 KI, ApoE3 KI, and ApoE4 KI[33] were used in this study. Non-sibling 20S-flag$^{flox/WT}$ mice were crossed to generate a homozygous 20S-flag$^{flox/flox}$ line. 20S-flag$^{flox/flox}$ were bred with neuronal Cre driver line BAF53b Cre to generate a 20S- flag$^{flox/flox}$ BAF53 line which expresses 20S-flag in neurons. hTau KI mice were crossed with ApoE2 KI, ApoE3 KI, and ApoE4 KI mice and homozygosed to generate homozygous hTau/ApoE2 KI, hTau/ApoE3 KI, and hTau/ApoE4 KI lines. Mice were genotyped using ear punches from weaning-age mice and tail snips from P0-1 pups post-mortem for primary neuron cultures. For the majority of experiments, mice were euthanized with carbon dioxide-induced anoxia and decapitated as a secondary method of euthanasia.

Generation of 20S-flag mice

20S-flag mice transgenic genomic sequence was designed in house, contracted out to Biocytogen Pharmaceuticals and generated using CRISPR/Cas9 editing. Zygotes were microinjected with Cas9-RNP complexes, selected for *in vitro,* and founders were identified by genotyping. F0 founders were crossed to produce F1s which were confirmed by genotyping and by southern blot analysis to confirm the lack of random integration and correct insertion of the target sequence into the endogenous locus.

Western blotting

Gels were run using the standard western blot protocol either on 10% Criterion TGX gels (Bio-Rad) or on 10% gels made in the laboratory. All antibodies were made up in a blocking buffer (5% BSA in 0.1% TBST). Western blots were imaged on a Licor Odyssey M Imager. Images were quantified using ImageStudio or ImageJ by standard densitometry analysis.

Cellular fractionation for plasma membrane enrichment

Cellular fractionation experiments were performed as previously described[3]. For cellular fractionation experiments with primary neurons, cultured neurons were lysed in a hypotonic lysis buffer (20 mM Tris pH 7.4, 5 mM NaCl, 2 mM $MgCl_2$, 0.2 mM $CaCl_2$, complete protease inhibitor cocktail tablet (Roche)) supplemented with 0.1% GDN and collected. Nuclei were pelleted at 1000 RPM, and the supernatant containing membranes was pelleted at 186,000 rcf. Pelleted membranes were washed twice by homogenizing in hypotonic lysis buffer and re-

pelleted. Following two washes, membranes were collected and prepared for SDS PAGE. For cellular fractionation with brain tissue, whole tissue from mouse brain was homogenized in hypotonic lysis buffer (20 mM Tris pH 7.4, 5 mM NaCl, 2 mM $MgCl_2$, 0.2 mM $CaCl_2$, complete protease inhibitor cocktail tablet). Nuclei were pelleted at 1000 RPM, and the pellet was washed in lysis buffer and re-pelleted. The supernatant containing membranes was brought up to 0.1% GDN and pelleted at 186,000 rcf. Pelleted membranes were washed twice by homogenizing in lysis buffer and re-pelleted. Following two washes, membranes were collected and prepared for SDS PAGE.

Surface Biotinylation and Streptavidin Pulldown

Surface biotin-labeling was performed as previously described[3]. Mouse brain tissue was recovered in cutting ACSF (195 mM sucrose, 10 mM NaCl, 15 mM glucose, 26 mM $NaHCO_3$, 2.5 mM KCl, 1.25 mM NaH_2PO_4, 0.5 mM $CaCl_2$, and 1 mM $MgCl_2$, bubbled with carbogen) at 4°C with light agitation for 30 minutes prior to biotin labeling. Mouse brain tissue and cultured neurons were washed in pH 8.0 cold PBS (Gibco) supplemented with 2 mM $MgCl_2$ and 0.1 mM $CaCl_2$ (PBSCM) and incubated in 0.5 mg/mL Sulfo-NHS-LC-Biotin (Thermo Fisher) dissolved in PBSCM at 4°C for 10 minutes. The labeling reaction was quenched in 50 mM glycine in two sequential 10-minute incubations at 4°C. Mouse brain tissue and cultured neurons were collected and homogenized in RIPA buffer (50 mM Tris pH 7.4, 250 mM NaCl, 1% Triton X-100, 0.5% Sodium Deoxycholate, 0.1% SDS, 5 mM EDTA, complete protease inhibitor cocktail tablet (Roche)). Samples were pelleted at 20,000 RCF for 10 minutes at 4°C and the supernatant was taken for streptavidin pulldown. For streptavidin pulldowns, lysate was incubated with high-capacity streptavidin agarose beads (ThermoFisher) overnight and washed 5 ties with RIPA buffer before elution in SDS sample buffer supplemented with 25 mM biotin.

LLVY-based proteasome activity assay

Chymotrypsin-like catalytic activity was assessed using a Suc-LLVY-AMC activity assay. Lysate was collected as described and diluted in activity assay buffer (25 mM Tris pH 7.4, 2.5 mM $MgCl_2$, and 10 mM NaCl) supplemented with 2 mM ATP. 10 mM Suc-LLVY-AMC (Enzo Life Sciences) was added to the diluted lysate, and proteasomal activity was assessed +/- 10 uM epoxomicin by measuring fluorescence intensity at 460 nm.

RAP Purification

Stable RAP expression plasmid was obtained from Kerafast (EMD008) and was transformed into T7 Express lysY Competent *E. coli* (NEB). *E. coli* containing the plasmid were cultured, induced with Isopropyl β-D-1-thiogalactopyranoside (Hello Bio), and incubated[30]. Cultures were pelleted and resuspended in Resuspension Buffer (50 mM Tris HCl, 50 mM EDTA, 15% sucrose, pH 8.0). Cells were lysed on ice in 1 mg/mL lysozyme (ThermoFIsher) and 1:1000 DNase (Worthington Biochemical). 0.02% TritonX-100 (v/v) and complete protease inhibitor cocktail tablets (Roche) were mixed into the lysate. Lysate was passed consecutively through 18 and 25 gauge needles and centrifuged. The supernatant was removed and incubated with Glutathione Sepharose resin (Cytiva). Beads were packed into a gravity column and washed with 5 column volumes in Buffer A (20 mM HEPES, 100 mM KCl, 0.2 mM EDTA, 5% glycerol, and complete protease inhibitor cocktail tablets). RAP-GST was eluted in Buffer A with 25 mM glutathione (Fisher Scientific). Fractions confirmed by Coomassie were dialyzed in a dialysis buffer (20 mM

HEPES, 50 mM NaCl, and 5% glycerol at pH 7.4) and incubated with Thrombin beads (Innovative Research). Beads were removed and RAP was purified using an AKTA pure with a Superdex 200 increase column (Cytiva) in SEC buffer (150 mM NaCl, 0.2 mM EDTA pH 8, and 10% glycerol). Fractions confirmed by Coomassie were concentrated using a 30 kDa MWCO filter and concentration was assessed using a BCA assay (ThermoFisher). RAP was stored in single use aliquots at -80°C.

Human Subjects

Human samples were obtained from MassGeneral Institute for Neurodegenerative Disease. The use of post-mortem brain tissue was approved by the Harvard University institutional review board (IRB). Informed consent was obtained from all subjects. The authors did not have access to any identifying personal information. Alzheimer's disease neuropathologic change rating was made using three criteria. Blind assessment for density of neuritic beta amyloid, distribution of beta amyloid plaques and Braak Tau stage were conducted using the scoring system recommended by the Consortium to Establish a Registry for Alzheimer's disease[88], Thal Score[89] and Bielchowsky's silver stain[90] along with total Tau immunostaining respectively. According to the Braak Tau pathway, the following brain regions were collected from 18 human patients from Braak I - Braak VI: the hippocampus, visual association area, entorhinal cortex, parietal associative area and primary motor area

The brains were sliced, flash frozen and dissection from BA4 and BA7 to be homogenized in lysis buffer (50 mM HEPES, 0.1 mM $CaCl_2$ and 2 mM $MgCl_2$, 100 mM NaCl) supplemented with fresh 1 mM ATP and 0.1% GDN (Anatrace). Nuclei and mitochondria were pelleted at 7500 RPM and washed several times. The supernatant containing the membranes was pelleted at 186,000 RCF, and the supernatant was taken as cytosol. Pelleted membranes were washed by homogenizing in lysis buffer and re-pelleted. After each wash, the supernatant was analyzed by LLVY-based proteasome activity assay to assess cleanliness of the prep. Following washes, plasma membrane and cytosolic fractions were prepared for mass spec and SDS PAGE.

Lipidated ApoE particles

Lipidated ApoE 2, 3, and 4 (PC-ApoE) were prepared from recombinant ApoE2, 3 and 4 (vendor) as previously described[91]. Samples were purified after lipidation using a superose 6 increase GL 10/300 columns using a buffer (20mM Phosphate buffer, 50mM NaCl, pH 7.4) at a flow rate of 0.5mL/min. To show negative stain images of the ApoE isoforms lipidated POPC and cholesterol, copper grids with carbon film were glow discharged and incubated with 30µL of sample. Samples were then washed 3 times with water and then stained with uranyl formate. Grids were blotted with a filter paper and imaged with a JOEL TEM microscope at 50k magnification (0.212492nm/pix).

Antibody feeding

Antibody feeding was performed as previously described[92]. On DIV13, neurons were treated with 400nM PC-ApoE. 24 hours later, hippocampal neurons were washed with PBS supplemented with 0.1 mM $CaCl_2$ and 2 mM $MgCl_2$ (PBSCM). On ice, hippocampal neurons were treated with Mouse anti-FLAG M2 antibodies (1:100) for treatment conditions, and

additionally with Chicken anti-MAP2 antibodies (1:100) and Rabbit anti-GluR1 antibodies (1:100) for controls. Antibodies were diluted in PBSCM supplemented with 1% BSA and incubated on live neurons. Antibodies were washed and neurons were rinsed in PBSCM. Neurons were fixed in 4% paraformaldehyde (Electron Microscopy Sciences)/4% sucrose and samples were blocked in 1X GDB (0.2 mM $NaPO_4$, 0.2% gelatin, 0.8M NaCl, and 0.1% TritonX-100). Chicken anti-MAP2 primary antibody was diluted as noted in 1X GDB and coverslips treated with PC-ApoE were incubated in primary dilutions. Coverslips were washed, incubated in secondary antibodies diluted 1:1000 in 1X GDB and washed again. Neurons were mounted on glass slices and imaged using a CSU-W1 SoRa confocal microscope. Images are representative maximal Z-projections of multiple optical sections. Images were quantified using ImageJ by integrated density analysis.

Sarkosyl extraction

For *in vitro* sarkosyl extractions, primary neurons were treated for 12 hours and lysed in sarkosyl lysis buffer (150 mM NaCl, 2 mM $MgCl_2$, 0.2 mM $CaCl_2$, 20 mM Tris pH 7.4, 1.5% n-laurylsarcosine (Sigma, 30% stock), protease inhibitors (Roche), and phosphatase inhibitors (Sigma)) and collected. Samples were pelleted at 23,000 rcf at 4°C for 10 minutes. The supernatants were collected as part of the sarkosyl-soluble fraction and pellets were resuspended in the sarkosyl lysis buffer. Samples were pelleted at 23,000 rcf at 4°C for 10 minutes and supernatants were collected and pooled with the sarkosyl-soluble fraction from the first spin. The pellets were taken as the sarkosyl-insoluble fractions, and resuspended in 6M urea, 2M thiourea. For *in vivo* sarkosyl extractions, mice were euthanized 72 hours following stereotactic intrahippocampal injections, the hippocampi were dissected out on ice and homogenized in a dounce homogenizer in the hypotonic lysis buffer. The lysate was then brought up to 1.5% n-laurylsarcosine and 250 mM NaCl, homogenized, and incubated at room temperature for 45 minutes. Samples were spun at 27,800 RCF at 4°C for 10 minutes with an additional sarkosyl buffer and the loose pellets were resuspended. Samples were pelleted at 27,800 RCF at 4°C for 10 minutes and supernatants were collected as the sarkosyl-soluble fraction. The pellets were taken as the sarkosyl-insoluble fractions, and resuspended in 6M urea, 2M thiourea.

Synthesis of iBEp

Impermeant Biotin-Epoxomicin (iBEp) was synthesized via Cu(I)-catalyzed alkyne-azide cycloaddition between Biotin-PEG4-alkyne (BroadPharm, catalog No. BP 22684) and Epoxomicin-PEG24-azide (Affinity Chemistry). 25 mM Biotin-PEG4-alkyne, resuspended in MilliQ water, was reacted 1:1 with 20 mM Epoxomicin-PEG24-azide, resuspended in DMSO. The Cu(I) catalyst was prepared by incubating 10 mM CuSO4 and 10 mM BTTES with 20 g/mL sodium ascorbate for a short period. Then, the Cu(I) catalyst mixture was added to the main reaction. The reaction was made up to the final volume by adding MilliQ water with 10% isopropyl alcohol. After reacting overnight with continuous stirring at RT, the reaction mixture was injected directly onto the Agilent ZORBAX Eclipse SB-C18 reverse-phase column (4.6 x 250 mm, 5 µm) for purification on the Agilent 1290 Infinity II LC system, 10-90% acetonitrile/water gradient. Product fractions were dried by vacuum evaporation and sent to Affinity Chemistry for analysis by LC-MS. Dried fractions were resuspended in DMSO and stored at -20°C.

Synthesis of SulfoMG-132

SulfoMG-132 was synthesized via strain-promoted alkyne-azide cycloaddition between DBCO-Sulfo-Link-Biotin (BroadPharm, catalog No. 22296) and MG-132-PEG24-azide (Affinity Chemistry). 25 mM DBCO-Sulfo-Link-Biotin was reacted 1:1 with 20 mM MG-132-PEG24-azide, both resuspended in MilliQ water. MilliQ water was added to make up to the final volume. The reaction was run overnight with continuous stirring at RT and purified using the same method as iBEp. Product fractions from the HPLC were dried by vacuum evaporation and sent to Affinity Chemistry for LC-MS analysis. Dried fractions were resuspended in MilliQ water and stored at 4°C.

Immunocytochemistry

Neurons were treated with iBEp, Epox, and/or CHX for 12 hours as described. After the treatment, neurons were washed with cold PBS supplemented with 0.1 mM $CaCl_2$ and 2 mM $MgCl_2$ (PBSCM) and fixed in 4% paraformaldehyde (Electron Microscopy Sciences)/4% sucrose for 8 minutes. Following fixation, neurons were washed 3 times in PBS. Coverslips were blocked in 1X GDB (0.2 mM $NaPO_4$, 0.2% gelatin, 0.8M NaCl, and 0.1% TritonX-100). Primary antibodies were diluted as noted in 1X GDB. After incubation, the coverslips were washed in PBS and incubated with secondary antibodies diluted 1:1000 in 1X GDB. Coverslips were washed in PBS and mounted and imaged using a CSU-W1 SoRa confocal microscope. Images are representative maximal Z-projections of multiple optical sections. Images were quantified using ImageJ by integrated density analysis.

Immunohistochemistry

72 hours following stereotactic intrahippocampal injections, mice were anesthetized with ketamine/xylazine and perfused with PBS before being perfused with 4% paraformaldehyde (PFA) (Electron Microscopy Sciences) diluted in PBS. Mice were decapitated and brains were removed and fixed in 4% PFA in PBS overnight. Brains were cryopreserved in sequential incubations with sucrose. Brains were embedded in OCT (Sakura) on dry ice, sectioned on a cryostat and collected on super frost glass slides (VWR). Sections were permeabilized in blocking buffer (10% normal goat serum (Vector Laboratories), 1% BSA in PBS) supplemented with 0.1% TritonX-100 and incubated in blocking buffer. Sections were incubated with primary antibodies Mouse anti-AT8 and Rabbit anti-NeuN diluted 1:1000 and with secondary antibodies diluted 1:1000. Sections were also stained with DAPI (ThermoFisher) diluted 1:1000 and submerged in 0.1% Sudan Black B (Sigma) in 70% ethanol to reduce autofluorescence. They were then mounted and imaged using a CSU-W1 SoRa confocal microscope. Images are representative maximal Z-projections of multiple optical sections. Images were quantified using ImageJ by integrated density analysis.

Stereotaxic Surgery

Mice were anesthetized with Avertin by weight through an intraperitoneal injection, given local and general painkillers Marcaine and Carprofen along with optical lube to prevent dryness. On the stereotax, the surgical site was shaved and prepared with 3 alternating rounds of betadine and ethanol washes. A vertical incision was made and the open skull area was swabbed with hydrogen peroxide to visualize bregma. The stereotactic equipment was centered on bregma and then adjusted via manipulators to ((+/-)2.5 mm laterally and 2.7mm posteriorly. A drill was used to open the holes in the skull on either hemisphere and a needle was lowered 2.2mm in order to inject into the hippocampus. The microinjector pump then delivered a dose of 2uL of the

drug/saline solution and retracted after a minute after delivery was complete. The wound was closed and sealed with VetBond.

Immunoprecipitation by affinity beads

Immunoprecipitation (IP) was performed in a batch format. For FLAG IP from the membrane protein extract, ChromoTek DYKDDDDK Fab-Trap™ Agarose resin (Proteintech) was equilibrated with LSB buffer. The extract from each brain along with about 75ul of beads was added to equilibrated beads and incubated with end-to-end rotation. The beads were washed and proteins were eluted with 2x SDS sample loading buffer.

FLAG IP from cytosolic fractions were performed similarly with the following modifications. About 50 µl beads slurry was equilibrated in the PD buffer (20 mM Tris-HCl, 100 mM NaCl, 2 mM MgCl2, 0.5 mM ATP) for each IP reaction. The IP reaction was then incubated and proteins were eluted with a 2x SDS sample loading buffer. UBL IP from cytosolic fractions were performed using UBPBio Rapid 26S proteasome Purification kit (UBPBio). The affinity beads were prepared by combining GST-Ubl with equilibrated glutathione agarose beads slurry for each IP reaction.

Mass Spectrometry

Mass spectrometry analysis was carried out in a data-dependent manner with a full scan in the mass-to-charge ratio (m/z) range of 350 to 1550 in the "Top Speed" setting, three seconds per cycle. MS1 and MS2 were acquired for the precursor ion detection and peptide fragmentation ion detection, respectively. MS1 scans were measured at a resolution of 120,000 at an m/z of 200. MS2 scans were acquired by fragmenting precursor ions using the higher-energy collisional dissociation (HCD) method and detected at a mass resolution of 50,000, at an m/z of 200. Automatic gain control for MS1 was set to one million ions and for MS2 was set to 0.05 million ions. A maximum ion injection time was set to 50 ms for MS1 and 100 ms for MS2. MS1 was acquired in profile mode and MS2 was acquired in centroid mode. Higher-energy collisional dissociation was set to 35 for MS2. Dynamic exclusion was set to 30 seconds, and singly-charged ions were rejected. Internal calibration was carried out using the lock mass option (m/z 445.1200025) from ambient air.

For the human sample proteomics, the details of the high resolution MS2 run were with Comet Search Parameters of 50 ppm for Peptide Mass Tolerance, 0.02 for Fragment Ion Tolerance, and 2 as the limit for Maximum Internal Cleavage site and Maximum differential per sites. The Reported Quant parameters were set to 0.003 for tolerance, 0 for ms3. The peak picking was set to max, number of isotopes were limited to 2 and MS2 isolation width was set to 0.9. The MS2 spectra were searched using the SEQUEST algorithm against a Uniprot composite database derived from the human proteasome containing its reversed complement and known contaminants. Peptide spectral matches were filtered to a 1% false discovery rate (FDR) using the target-decoy strategy combined with linear discriminant analysis and the proteins were filtered to a <1% FDR. The proteins were quantified only from peptides with a summed SN threshold of >100. Isolation specificity was set to be greater than 0.7.

For quantitative phospho-proteomics, MS2 spectra were searched using the COMET algorithm against a Uniprot composite database derived from the mouse proteome containing its reversed

complement and known contaminants. Phosphorylation of Ser, Thr and Tyr residues was set as a differential modification. Peptide spectral matches of phosphorylated peptides were filtered to a 1% false discovery rate (FDR) using the target-decoy strategy combined with linear discriminant analysis and the proteins were filtered to a <1% FDR. The proteins were quantified only from peptides with a summed SN threshold of >150. Isolation specificity was set to be greater than 0.5. A summary of the results for tc-762p not including contaminants and reverse hits lists Quantified Phos Peptide value to be 29,164 and Unique Quantified Peptide Value to be 12,814.
The combined sample was resuspended in Buffer A (5%ACN, 50mM AmBic, pH 8.0) and Basic pH reverse phase (bRP) phos sample offline fractionated into a 96-well plate. This plate was run by columns for a total of 12 final fractions, which were dried by speedvac, cleaned on a C18 packed stage tip and then eluted and resuspended in 5% ACN, 5% formic acid. These samples were analyzed by LC-MS2 on an Orbitrap Eclipse mass Spectrometer using a 180 minute high-rez MS2 method. Peptides were detected (MS1) and quantified (MS2).

Similar to the process just mentioned above, for the rest of the proteomics, combined samples were resuspended in Buffer A and offline fractionated. The 96 well plate was combined in checkerboard fashion for a total of 24 final fractions. 12 fractions were dried by speedvac, cleaned on a C18 packed stage tip and eluted. Samples were then resuspended in 5% ACN, 5% formic acid and analyzed by LC-MS3 using a real time search, data dependent method. 12 fractions from the total proteome HPRP set were analyzed on an Orbitrap Lumos mass spectrometer using a 150 minute method with real-time search. Peptides were detected (MS1) and quantified (MS3) in the Orbitrap and sequenced (MS2) in the ion trap. The MS2 spectra were searched using the COMET algorithm against a Uniprot composite database derived from the mouse proteome containing its reversed complement and known contaminants. The proteins from the 12 runs were filtered to a 1% false discovery rate (FDR) using the target-decoy strategy combined with linear discriminant analysis and were filtered to a <1% FDR. The proteins were quantified only from peptides with a summed SN threshold of >150. A summary of the results for tc-762p not including contaminants and reverse hits lists Quantified Proteins to be 8,681 and Quantified Peptides as 72,113. The Total Collapsed Proteins were 8,714.

Statistics

No statistical methods were used to predetermine sample size. The experiments were not randomized except for ApoE-KI surface biotinylation and cellular fractionation with postmortem patient tissues. All statistical analyses were performed using Origin Prism and Graphpad software except for mass spectrometry analysis which was analyzed using Bioconductor DEqMS[93], accounting for appropriate distribution and variance to ensure proper statistical parameters were applied. Experimental sample sizes were chosen according to norms within the field. The observed magnitude of differences, together with the low replicate variance, permits high power of analysis based on the sample size chosen. Statistical analysis using Student's t tests, 2-way ANOVAs, paired t-tests and the appropriate post hoc tests were performed as described in each figure legend. P values ≤ 0.05 were considered significant unless otherwise noted.

Microscopes

All images were acquired with a Nikon Ti2-E stand and CSU-W1 or CSU-W1 SoRa spinning disks with ORCA-fusionBT Hamamatsu cameras.

Commercial Drugs

Epoxomicin (Selleckchem) was used to treat cultured neurons at 10 uM, MG132 ((Selleckchem) was used to treat cultured neurons at 10 uM, and Cycloheximide (Sigma) was used to treat cultured neurons at 10 µg/mL.

1 Finkbeiner, S. The Autophagy Lysosomal Pathway and Neurodegeneration. *Cold Spring Harb Perspect Biol* **12**, doi:10.1101/cshperspect.a033993 (2020).

2 Collins, G. A. & Goldberg, A. L. The Logic of the 26S Proteasome. *Cell* **169**, 792-806, doi:10.1016/j.cell.2017.04.023 (2017).

3 Ramachandran, K. V. & Margolis, S. S. A mammalian nervous-system-specific plasma membrane proteasome complex that modulates neuronal function. *Nat Struct Mol Biol* **24**, 419-430, doi:10.1038/nsmb.3389 (2017).

4 Ramachandran, K. V. *et al.* Activity-Dependent Degradation of the Nascentome by the Neuronal Membrane Proteasome. *Mol Cell* **71**, 169-177 e166, doi:10.1016/j.molcel.2018.06.013 (2018).

5 Labbadia, J. & Morimoto, R. I. The biology of proteostasis in aging and disease. *Annu Rev Biochem* **84**, 435-464, doi:10.1146/annurev-biochem-060614-033955 (2015).

6 Ross, C. A. & Poirier, M. A. Protein aggregation and neurodegenerative disease. *Nat Med* **10 Suppl**, S10-17, doi:10.1038/nm1066 (2004).

7 Chung, D. C., Roemer, S., Petrucelli, L. & Dickson, D. W. Cellular and pathological heterogeneity of primary tauopathies. *Mol Neurodegener* **16**, 57, doi:10.1186/s13024-021-00476-x (2021).

8 Glasauer, S. M. K. *et al.* Human tau mutations in cerebral organoids induce a progressive dyshomeostasis of cholesterol. *Stem Cell Reports* **17**, 2127-2140, doi:10.1016/j.stemcr.2022.07.011 (2022).

9 Clavaguera, F. *et al.* Brain homogenates from human tauopathies induce tau inclusions in mouse brain. *Proc Natl Acad Sci U S A* **110**, 9535-9540, doi:10.1073/pnas.1301175110 (2013).

10 Clavaguera, F. *et al.* Transmission and spreading of tauopathy in transgenic mouse brain. *Nat Cell Biol* **11**, 909-913, doi:10.1038/ncb1901 (2009).

11 Sanders, D. W. *et al.* Distinct tau prion strains propagate in cells and mice and define different tauopathies. *Neuron* **82**, 1271-1288, doi:10.1016/j.neuron.2014.04.047 (2014).

12 Dujardin, S. *et al.* Different tau species lead to heterogeneous tau pathology propagation and misfolding. *Acta Neuropathol Commun* **6**, 132, doi:10.1186/s40478-018-0637-7 (2018).

13 Xia, D., Gutmann, J. M. & Gotz, J. Mobility and subcellular localization of endogenous, gene-edited Tau differs from that of over-expressed human wild-type and P301L mutant Tau. *Sci Rep* **6**, 29074, doi:10.1038/srep29074 (2016).
14 Tracy, T. E. *et al.* Tau interactome maps synaptic and mitochondrial processes associated with neurodegeneration. *Cell* **185**, 712-728.e714, doi:10.1016/j.cell.2021.12.041 (2022).
15 Kamath, T. V. *et al.* Kinetics of tau aggregation reveals patient-specific tau characteristics among Alzheimer's cases. *Brain Commun* **3**, fcab096, doi:10.1093/braincomms/fcab096 (2021).
16 Jouanne, M., Rault, S. & Voisin-Chiret, A. S. Tau protein aggregation in Alzheimer's disease: An attractive target for the development of novel therapeutic agents. *Eur J Med Chem* **139**, 153-167, doi:10.1016/j.ejmech.2017.07.070 (2017).
17 Keck, S., Nitsch, R., Grune, T. & Ullrich, O. Proteasome inhibition by paired helical filament-tau in brains of patients with Alzheimer's disease. *J Neurochem* **85**, 115-122, doi:10.1046/j.1471-4159.2003.01642.x (2003).
18 Myeku, N. *et al.* Tau-driven 26S proteasome impairment and cognitive dysfunction can be prevented early in disease by activating cAMP-PKA signaling. *Nat Med* **22**, 46-53, doi:10.1038/nm.4011 (2016).
19 Kruger, U., Wang, Y., Kumar, S. & Mandelkow, E. M. Autophagic degradation of tau in primary neurons and its enhancement by trehalose. *Neurobiol Aging* **33**, 2291-2305, doi:10.1016/j.neurobiolaging.2011.11.009 (2012).
20 Lei, Z., Brizzee, C. & Johnson, G. V. BAG3 facilitates the clearance of endogenous tau in primary neurons. *Neurobiol Aging* **36**, 241-248, doi:10.1016/j.neurobiolaging.2014.08.012 (2015).
21 Feuillette, S. *et al.* Tau is not normally degraded by the proteasome. *J Neurosci Res* **80**, 400-405, doi:10.1002/jnr.20414 (2005).
22 Fan, W. *et al.* NPAS4 Facilitates the Autophagic Clearance of Endogenous Tau in Rat Cortical Neurons. *J Mol Neurosci* **58**, 401-410, doi:10.1007/s12031-015-0692-5 (2016).
23 Saha, I. *et al.* The AAA+ chaperone VCP disaggregates Tau fibrils and generates aggregate seeds. *bioRxiv*, 2022.2002.2018.481043, doi:10.1101/2022.02.18.481043 (2022).
24 Dincer, A. *et al.* APOE epsilon4 genotype, amyloid-beta, and sex interact to predict tau in regions of high APOE mRNA expression. *Sci Transl Med* **14**, eabl7646, doi:10.1126/scitranslmed.abl7646 (2022).
25 Shi, Y. *et al.* ApoE4 markedly exacerbates tau-mediated neurodegeneration in a mouse model of tauopathy. *Nature* **549**, 523-527, doi:10.1038/nature24016 (2017).
26 Baek, M. S. *et al.* Effect of APOE epsilon4 genotype on amyloid-beta and tau accumulation in Alzheimer's disease. *Alzheimers Res Ther* **12**, 140, doi:10.1186/s13195-020-00710-6 (2020).
27 Strittmatter, W. J. *et al.* Apolipoprotein E: high-avidity binding to beta-amyloid and increased frequency of type 4 allele in late-onset familial Alzheimer disease. *Proc Natl Acad Sci U S A* **90**, 1977-1981, doi:10.1073/pnas.90.5.1977 (1993).
28 Holtzman, D. M., Herz, J. & Bu, G. Apolipoprotein E and apolipoprotein E receptors: normal biology and roles in Alzheimer disease. *Cold Spring Harb Perspect Med* **2**, a006312, doi:10.1101/cshperspect.a006312 (2012).
29 Zhan, X. *et al.* Generation of BAF53b-Cre transgenic mice with pan-neuronal Cre activities. *Genesis* **53**, 440-448, doi:10.1002/dvg.22866 (2015).

30 Prasad, J. M., Migliorini, M., Galisteo, R. & Strickland, D. K. Generation of a Potent Low Density Lipoprotein Receptor-related Protein 1 (LRP1) Antagonist by Engineering a Stable Form of the Receptor-associated Protein (RAP) D3 Domain. *J Biol Chem* **290**, 17262-17268, doi:10.1074/jbc.M115.660084 (2015).
31 Laatsch, A. *et al.* Low density lipoprotein receptor-related protein 1 dependent endosomal trapping and recycling of apolipoprotein E. *PLoS One* **7**, e29385, doi:10.1371/journal.pone.0029385 (2012).
32 Lee, D. *et al.* RAP uses a histidine switch to regulate its interaction with LRP in the ER and Golgi. *Mol Cell* **22**, 423-430, doi:10.1016/j.molcel.2006.04.011 (2006).
33 Huynh, T. V. *et al.* Lack of hepatic apoE does not influence early Abeta deposition: observations from a new APOE knock-in model. *Mol Neurodegener* **14**, 37, doi:10.1186/s13024-019-0337-1 (2019).
34 Yan, S. *et al.* Sex modifies APOE epsilon4 dose effect on brain tau deposition in cognitively impaired individuals. *Brain* **144**, 3201-3211, doi:10.1093/brain/awab160 (2021).
35 Yan, S. *et al.* Association of sex and APOE epsilon4 with brain tau deposition and atrophy in older adults with Alzheimer's disease. *Theranostics* **10**, 10563-10572, doi:10.7150/thno.48522 (2020).
36 Oveisgharan, S. *et al.* Sex differences in Alzheimer's disease and common neuropathologies of aging. *Acta Neuropathol* **136**, 887-900, doi:10.1007/s00401-018-1920-1 (2018).
37 Mazure, C. M. & Swendsen, J. Sex differences in Alzheimer's disease and other dementias. *Lancet Neurol* **15**, 451-452, doi:10.1016/S1474-4422(16)00067-3 (2016).
38 Lane-Donovan, C. & Herz, J. ApoE, ApoE Receptors, and the Synapse in Alzheimer's Disease. *Trends Endocrinol Metab* **28**, 273-284, doi:10.1016/j.tem.2016.12.001 (2017).
39 Verghese, P. B. *et al.* ApoE influences amyloid-beta (Abeta) clearance despite minimal apoE/Abeta association in physiological conditions. *Proc Natl Acad Sci U S A* **110**, E1807-1816, doi:10.1073/pnas.1220484110 (2013).
40 Kim, M. J., Dunah, A. W., Wang, Y. T. & Sheng, M. Differential roles of NR2A- and NR2B-containing NMDA receptors in Ras-ERK signaling and AMPA receptor trafficking. *Neuron* **46**, 745-760, doi:10.1016/j.neuron.2005.04.031 (2005).
41 Hanley, J. G., Khatri, L., Hanson, P. I. & Ziff, E. B. NSF ATPase and alpha-/beta-SNAPs disassemble the AMPA receptor-PICK1 complex. *Neuron* **34**, 53-67 (2002).
42 Manral, P. *et al.* Can apolipoproteins and complement factors be biomarkers of Alzheimer's disease? *Curr Alzheimer Res* **9**, 935-943, doi:10.2174/156720512803251110 (2012).
43 Xu, B. *et al.* A quantitative proteomic analysis reveals the potential roles of PRDX3 in neurite outgrowth in N2a-APPswe cells. *Biochem Biophys Res Commun* **604**, 144-150, doi:10.1016/j.bbrc.2022.03.021 (2022).
44 Oeckl, P. *et al.* Proteomics in cerebrospinal fluid and spinal cord suggests UCHL1, MAP2 and GPNMB as biomarkers and underpins importance of transcriptional pathways in amyotrophic lateral sclerosis. *Acta Neuropathol* **139**, 119-134, doi:10.1007/s00401-019-02093-x (2020).
45 Rayaprolu, S. *et al.* Systems-based proteomics to resolve the biology of Alzheimer's disease beyond amyloid and tau. *Neuropsychopharmacology* **46**, 98-115, doi:10.1038/s41386-020-00840-3 (2021).

46 Beckmann, N. D. *et al.* Multiscale causal networks identify VGF as a key regulator of Alzheimer's disease. *Nat Commun* **11**, 3942, doi:10.1038/s41467-020-17405-z (2020).
47 Yin, Z. *et al.* Detecting Prognosis Risk Biomarkers for Colon Cancer Through Multi-Omics-Based Prognostic Analysis and Target Regulation Simulation Modeling. *Front Genet* **11**, 524, doi:10.3389/fgene.2020.00524 (2020).
48 Villa, C., Suphesiz, H., Combi, R. & Akyuz, E. Potassium channels in the neuronal homeostasis and neurodegenerative pathways underlying Alzheimer's disease: An update. *Mech Ageing Dev* **185**, 111197, doi:10.1016/j.mad.2019.111197 (2020).
49 Meng, L. *et al.* Epoxomicin, a potent and selective proteasome inhibitor, exhibits in vivo antiinflammatory activity. *Proc Natl Acad Sci U S A* **96**, 10403-10408 (1999).
50 Sin, N. *et al.* Total synthesis of the potent proteasome inhibitor epoxomicin: a useful tool for understanding proteasome biology. *Bioorg Med Chem Lett* **9**, 2283-2288 (1999).
51 Xin, B. T. *et al.* Two-Step Bioorthogonal Activity-Based Protein Profiling of Individual Human Proteasome Catalytic Sites. *Chembiochem* **21**, 248-255, doi:10.1002/cbic.201900551 (2020).
52 Kisselev, A. F., van der Linden, W. A. & Overkleeft, H. S. Proteasome inhibitors: an expanding army attacking a unique target. *Chem Biol* **19**, 99-115, doi:10.1016/j.chembiol.2012.01.003 (2012).
53 Pye, C. R. *et al.* Nonclassical Size Dependence of Permeation Defines Bounds for Passive Adsorption of Large Drug Molecules. *J Med Chem* **60**, 1665-1672, doi:10.1021/acs.jmedchem.6b01483 (2017).
54 Matsson, P. & Kihlberg, J. How Big Is Too Big for Cell Permeability? *J Med Chem* **60**, 1662-1664, doi:10.1021/acs.jmedchem.7b00237 (2017).
55 Soriano, G. P., Overkleeft, H. S. & Florea, B. I. Two-Step Activity-Based Protein Profiling with the Proteasome System as Model of Study. *Methods Mol Biol* **1491**, 205-215, doi:10.1007/978-1-4939-6439-0_15 (2017).
56 Li, N. *et al.* Relative quantification of proteasome activity by activity-based protein profiling and LC-MS/MS. *Nat Protoc* **8**, 1155-1168, doi:10.1038/nprot.2013.065 (2013).
57 Sha, Z., Schnell, H. M., Ruoff, K. & Goldberg, A. Rapid induction of p62 and GABARAPL1 upon proteasome inhibition promotes survival before autophagy activation. *Journal of Cell Biology* **217**, 1757-1776, doi:10.1083/jcb.201708168 (2018).
58 Colledge, M. *et al.* Ubiquitination regulates PSD-95 degradation and AMPA receptor surface expression. *Neuron* **40**, 595-607, doi:10.1016/s0896-6273(03)00687-1 (2003).
59 Gao, J. *et al.* The E3 ubiquitin ligase IDOL regulates synaptic ApoER2 levels and is important for plasticity and learning. *eLife* **6**, e29178, doi:10.7554/eLife.29178 (2017).
60 Hung, A. Y., Sung, C. C., Brito, I. L. & Sheng, M. Degradation of postsynaptic scaffold GKAP and regulation of dendritic spine morphology by the TRIM3 ubiquitin ligase in rat hippocampal neurons. *PLoS One* **5**, e9842, doi:10.1371/journal.pone.0009842 (2010).
61 Yoshii, S. R. & Mizushima, N. Monitoring and Measuring Autophagy. *International Journal of Molecular Sciences* **18**, 1865 (2017).
62 Guo, Q. *et al.* Targeted Quantification of Detergent-Insoluble RNA-Binding Proteins in Human Brain Reveals Stage and Disease Specific Co-aggregation in Alzheimer's Disease. *Front Mol Neurosci* **14**, 623659, doi:10.3389/fnmol.2021.623659 (2021).
63 Hales, C. M. *et al.* Changes in the detergent-insoluble brain proteome linked to amyloid and tau in Alzheimer's Disease progression. *Proteomics* **16**, 3042-3053, doi:10.1002/pmic.201600057 (2016).

64 Maziuk, B. F. *et al.* RNA binding proteins co-localize with small tau inclusions in tauopathy. *Acta Neuropathologica Communications* **6**, 71, doi:10.1186/s40478-018-0574-5 (2018).
65 Vanderweyde, T. *et al.* Interaction of tau with the RNA-Binding Protein TIA1 Regulates tau Pathophysiology and Toxicity. *Cell Rep* **15**, 1455-1466, doi:10.1016/j.celrep.2016.04.045 (2016).
66 Saito, T. *et al.* Humanization of the entire murine Mapt gene provides a murine model of pathological human tau propagation. *J Biol Chem* **294**, 12754-12765, doi:10.1074/jbc.RA119.009487 (2019).
67 Guo, J. L. *et al.* Unique pathological tau conformers from Alzheimer's brains transmit tau pathology in nontransgenic mice. *J Exp Med* **213**, 2635-2654, doi:10.1084/jem.20160833 (2016).
68 Wang, J. Z., Xia, Y. Y., Grundke-Iqbal, I. & Iqbal, K. Abnormal hyperphosphorylation of tau: sites, regulation, and molecular mechanism of neurofibrillary degeneration. *J Alzheimers Dis* **33 Suppl 1**, S123-139, doi:10.3233/jad-2012-129031 (2013).
69 Alonso, A. D. *et al.* Hyperphosphorylation of Tau Associates With Changes in Its Function Beyond Microtubule Stability. *Front Cell Neurosci* **12**, 338, doi:10.3389/fncel.2018.00338 (2018).
70 Alpaugh, M. *et al.* Passive immunization against phosphorylated tau improves features of Huntington's disease pathology. *Mol Ther* **30**, 1500-1522, doi:10.1016/j.ymthe.2022.01.020 (2022).
71 Cao, L. *et al.* Pseudo-phosphorylation at AT8 epitopes regulates the tau truncation at aspartate 421. *Exp Cell Res* **370**, 103-115, doi:10.1016/j.yexcr.2018.06.010 (2018).
72 Quintanilla, R. A., von Bernhardi, R., Godoy, J. A., Inestrosa, N. C. & Johnson, G. V. Phosphorylated tau potentiates Aβ-induced mitochondrial damage in mature neurons. *Neurobiol Dis* **71**, 260-269, doi:10.1016/j.nbd.2014.08.016 (2014).
73 Wang, X. *et al.* T217-Phosphorylation Exacerbates Tau Pathologies and Tau-Induced Cognitive Impairment. *J Alzheimers Dis* **81**, 1403-1418, doi:10.3233/jad-210297 (2021).
74 Subramanian, M. *et al.* UBE4B, a microRNA-9 target gene, promotes autophagy-mediated Tau degradation. *Nat Commun* **12**, 3291, doi:10.1038/s41467-021-23597-9 (2021).
75 Ndoja, A. *et al.* Ubiquitin Ligase COP1 Suppresses Neuroinflammation by Degrading c/EBPβ in Microglia. *Cell* **182**, 1156-1169.e1112, doi:10.1016/j.cell.2020.07.011 (2020).
76 Rousseau, A. & Bertolotti, A. Regulation of proteasome assembly and activity in health and disease. *Nat Rev Mol Cell Biol* **19**, 697-712, doi:10.1038/s41580-018-0040-z (2018).
77 VerPlank, J. J. S. & Goldberg, A. L. Regulating protein breakdown through proteasome phosphorylation. *Biochem J* **474**, 3355-3371, doi:10.1042/bcj20160809 (2017).
78 Lee, S. *et al.* PTK2/FAK regulates UPS impairment via SQSTM1/p62 phosphorylation in TARDBP/TDP-43 proteinopathies. *Autophagy* **16**, 1396-1412, doi:10.1080/15548627.2019.1686729 (2020).
79 Erales, J. & Coffino, P. Ubiquitin-independent proteasomal degradation. *Biochim Biophys Acta* **1843**, 216-221, doi:10.1016/j.bbamcr.2013.05.008 (2014).
80 Schmidt, M. F., Gan, Z. Y., Komander, D. & Dewson, G. Ubiquitin signalling in neurodegeneration: mechanisms and therapeutic opportunities. *Cell Death Differ* **28**, 570-590, doi:10.1038/s41418-020-00706-7 (2021).

81 Rape, M. Ubiquitylation at the crossroads of development and disease. *Nat Rev Mol Cell Biol* **19**, 59-70, doi:10.1038/nrm.2017.83 (2018).
82 Salazar-Chaparro, A. F., Halder, S. & Trader, D. J. Synthesis and Application of a Clickable Epoxomicin-Based Probe for Proteasome Activity Analysis. *Curr Protoc* **2**, e490, doi:10.1002/cpz1.490 (2022).
83 Getz, G. S. & Reardon, C. A. Apoprotein E and Reverse Cholesterol Transport. *Int J Mol Sci* **19**, doi:10.3390/ijms19113479 (2018).
84 Wang, Y. *et al.* The release and trans-synaptic transmission of Tau via exosomes. *Mol Neurodegener* **12**, 5, doi:10.1186/s13024-016-0143-y (2017).
85 Wu, J. W. *et al.* Neuronal activity enhances tau propagation and tau pathology in vivo. *Nat Neurosci* **19**, 1085-1092, doi:10.1038/nn.4328 (2016).
86 Serrano-Pozo, A., Das, S. & Hyman, B. T. APOE and Alzheimer's disease: advances in genetics, pathophysiology, and therapeutic approaches. *Lancet Neurol* **20**, 68-80, doi:10.1016/s1474-4422(20)30412-9 (2021).
87 Dawson, H. N. *et al.* Inhibition of neuronal maturation in primary hippocampal neurons from tau deficient mice. *J Cell Sci* **114**, 1179-1187, doi:10.1242/jcs.114.6.1179 (2001).
88 Morris, J. C. *et al.* The Consortium to Establish a Registry for Alzheimer's Disease (CERAD). Part I. Clinical and neuropsychological assessment of Alzheimer's disease. *Neurology* **39**, 1159-1165, doi:10.1212/wnl.39.9.1159 (1989).
89 Thal, D. R., Rüb, U., Orantes, M. & Braak, H. Phases of A beta-deposition in the human brain and its relevance for the development of AD. *Neurology* **58**, 1791-1800, doi:10.1212/wnl.58.12.1791 (2002).
90 Braak, H. & Braak, E. Neuropathological stageing of Alzheimer-related changes. *Acta Neuropathol* **82**, 239-259, doi:10.1007/bf00308809 (1991).
91 Verghese, P. B. *et al.* ApoE influences amyloid-β (Aβ) clearance despite minimal apoE/Aβ association in physiological conditions. *Proc Natl Acad Sci U S A* **110**, E1807-1816, doi:10.1073/pnas.1220484110 (2013).
92 Ascaño, M., Richmond, A., Borden, P. & Kuruvilla, R. Axonal targeting of Trk receptors via transcytosis regulates sensitivity to neurotrophin responses. *J Neurosci* **29**, 11674-11685, doi:10.1523/jneurosci.1542-09.2009 (2009).
93 Zhu, Y. Bioconductor-DEqMS: A Tool to Perform Statistical Analysis of Differential Protein Expression for Quantitative Proteomics Data. *R package version* **1**, 10.18129 (2019).